THE LARGE-SCALE RESPONSE OF THE TROPICAL ATMOSPHERE TO RADIATIVE HEATING

by Bruce A. Albrecht
Stephen K. Cox

Atmospheric Science
PAPER NO.
215

US ISSN 0067-0340

DEPARTMENT OF ATMOSPHERIC SCIENCE
COLORADO STATE UNIVERSITY
FORT COLLINS, COLORADO

THE LARGE-SCALE RESPONSE OF THE TROPICAL ATMOSPHERE TO RADIATIVE HEATING

by

Bruce A. Albrecht

and

Stephen K. Cox

This report was prepared with support from
The National Science Foundation
Grant No. GA-36302

Department of Atmospheric Science
Colorado State University
Fort Collins, Colorado

March 1974

Atmospheric Science Paper No. 215

ABSTRACT

A large-scale diagnostic model is used to determine the effect of various diabatic forcing functions on tropospheric motions. In this model the diabatic heating is specified and the response of the atmosphere to this forcing is determined. Many of the features of the tropospheric equatorial waves are duplicated by using the observed difference in heating between the trough and the ridge of the waves in the model.

The structure of waves forced by the observed differences in radiative heating was determined. Although the atmospheric response to this heating showed little resemblance to the observed wave structure, it was similar to the layered meridional wind structure observed during the Line Island Experiment. When the radiative heating was combined with convective heating, the vertical structure of the forced motions was found to be very sensitive to the phase difference of the convective and the radiative heating. The amplitude of the meridional wind perturbations at 200 mb varied from 1 m sec^{-1} for the case when radiatively active upper tropospheric clouds were centered over the convective heating to 5.5 m sec^{-1} when the cloud was centered a half of wavelength from the convective heating. For the same cloud configurations, the divergence at 200 mb varied from 1×10^{-6} sec^{-1} to $8 \times 10^{-6} sec^{-1}$ at the region of the maximum convective heating. The variation of the response due to vertical shear of the mean zonal wind is determined.

ACKNOWLEDGEMENTS

We would like to express our gratitude to Dr. Wayne Schubert for his many helpful discussions and suggestions in this research project.

This research has been supported by the Atmospheric Science Section of the National Science Foundation under Grant GA-36302.

TABLE OF CONTENTS

LIST OF FIGURES

LIST OF FIGURES - Continued

LIST OF FIGURES - Continued

LIST OF SYMBOLS

a	radius of the earth
C_p	specific heat of dry air at constant pressure
D	dimensionless dissipation coefficient, $\kappa(2\Omega)^{-1}$
H	vertical height scale
$H_B(\uparrow)$	upward irradiance at cloud base
$H_B(\downarrow)$	downward irradiance at cloud base
$H_T(\uparrow)$	upward irradiance at cloud top
$H_T(\downarrow)$	Downward irradiance at cloud top
k	dimensionless zonal wave number
p	pressure
p_o	sea level reference pressure
Q	diabatic heating per unit mass
Q_1	apparent heat source
Q_c	convective heating
Q_R	radiative heating
Q_{RM}	mean infrared heating
Q^*	dimensionless diabatic heating
Q'	amplitude of the sinusoidal heating
R	gas constant for dry air
S	dimensionless static stability
t	time
t^*	dimensionless time
T	temperature perturbation
$\overline{T}$	time-zonally averaged zonal temperature
T^*	dimensionless temperature perturbation
T'	amplitude of the sinusoidal temperature perturbations

T_{CT}	temperature of the cloud top
T_{CB}	temperature of the cloud bottom
u	zonal velocity perturbation
$\bar{u}$	time-zonally averaged zonal velocity
$\bar{u}^*$	nondimensional time-zonally averaged zonal wind
u^*	nondimensional zonal velocity perturbation
u'	amplitude of the sinusoidal zonal velocity perturbation
u_o	$\bar{u}^*(1-y^2)$
v	meridional velocity perturbation
v^*	nondimensional meridional velocity perturbation
v'	amplitude of the sinusoidal meridional velocity perturbation
w	pseudo-height vertical velocity perturbation
w^*	nondimensional pseudo-height vertical velocity perturbation
w'	amplitude of the sinusoidal pseudo-height vertical velocity perturbation
y_c	sin of the latitude of maximum convective heating
y_r	sin of the latitude of maximum radiative heating
z	height above sea level surface
α_c	parameter used to specify the latitudinal width of the convective heating
α_r	parameter used to specify the latitudinal width of the radiative heating
$\varepsilon^*(\uparrow)$	upward effective emissivity
$\varepsilon^*(\downarrow)$	downward effective emissivity
κ	Rayleigh drag coefficient, rate coefficient for Newtonian cooling
λ	longitude

ω	dimensionless frequency
$\hat{\omega}$	$\omega + \frac{k\bar{u}}{1-y^2} - iD$
ϕ	latitude
Φ	geopotential height perturbation
Φ^*	dimensionless geopotential height perturbation
Φ'	amplitude of sinusoidal geopotential height perturbations
σ	Stefan-Boltzman constant
σ	$-\frac{S}{\hat{\omega}} \frac{d}{d\xi} (\frac{\hat{\omega}}{S})$
θ	phase angle between the convective and radiative heating
ξ	pseudo-height vertical coordinate
ξ^*	dimensionless pseudo-height vertical component

I. INTRODUCTION

Horizontal differences in the diabatic heating force large-scale motions in the tropical atmosphere. The principal components of the diabatic heating are the heating caused by the release of latent heat in cumulus clouds and the radiative heating.

The release of latent heat in cumulus clouds results in an increased buoyancy of the cloud parcels, and hence, an increase upward mass transport. A compensating downward motion must occur in the environment. From a large-scale point of view, Gray (1972) and Yanai et al.(1973) have shown that the net effect of this process will be a heating of the environment.

Horizontal gradients in the convective heating result from the spatial distribution of convective clouds. Reed and Recker (1972) and Yanai et al.(1973) have made calculations of the large-scale convective heating. A known radiative heating, however, is implicitly required for these measurements.

The radiative heating of the atmosphere depends on the net divergence of the shortwave (.3 μm - 3 μm) and infrared (3 μm - 100 μm) radiation. Although water vapor, carbon dioxide, and ozone content are important in determining the radiative heating of the atmosphere, clouds are the principle modulators of this heating. Consequently, horizontal variations in the cloudiness result in horizontal gradients of the radiative heating.

The effects of clouds on infrared heating has been determined from measurements made during the Line Island Experiment (LIE), 1967 (Cox, 1969b). Of particular interest is the infrared heating resulting from an upper tropospheric cloud layer (eg. cirrostratus and altostratus)

occurring every six to eight days during the LIE. The vertical heating profile resulting from this cloud configuration differs significantly from the profile observed for other cloud configurations and for clear sky conditions. The differences are as large as 4^{o} C day^{-1} at individual levels, which is the same order of magnitude as the horizontal differences in the large-scale convective heating.

Spectral analysis studies made of the wind, temperature, and moisture fields in the tropics indicate the presence of wave motions in both the lower and upper troposphere (see Wallace, 1971 for a comprehensive survey). Hayashi (1970), Holton (1971), Wallace (1971) and others have suggested that the diabatic heating resulting from the precipitation systems imbedded within these waves is a source of energy for the waves. Reed and Recker (1971) using a compositing technique determined a maximum in the rainfall near the trough of the lower tropospheric wave system.

Chang (1970) and Wallace (1970) used satellite photographs in the form of time-longitude sections to reveal temporal and spatial variations in the tropical cloudiness which have the same time and space scales as the observed wave motions. Reed and Recker (1971) using similar photographs were able to correlate the variations in the cloudiness with lower tropospheric wave motions. The horizontal differences in cloudiness indicated by these photographs may result in horizontal differences in the radiative heating, particularly if the satellite observed cloudiness consists of upper tropospheric clouds. The persistence in time and the areal extent of this cloudiness would indicate that the radiative heating may be an important component of the total diabatic heating differences occurring within the wave systems.

Holton (1971) developed a diagnostic wave model to determine the response of the atmosphere to a prescribed diabatic forcing. Using a rather crude representation of the heating, he was able to successfully duplicate many of the features of the observed wave motions.

In this study, the model formulated by Holton (1971) is used to determine the sensitivity of the tropical atmosphere to variations in the diabatic heating. The response of the atmosphere to radiative forcing only is deduced using this large-scale diagnostic model. The variations in the wave structure which result from phase differences in the radiative and convective heating are determined. The effect of vertical shear of the mean zonal wind on the response is also studied.

II. LARGE-SCALE DIABATIC HEATING

The diabatic heating distribution must be specified as a known variable in the diagnostic wave model developed below. It is desirable to specify the radiative and convective heating as separate quantities since these quantities may have varying spatial distributions. In this section, radiative and convective heating profiles which are consistent with observations will be specified.

A. Radiative Heating

The net divergence of longwave radiation is the principal source of radiative heating (cooling equals negative heating) in the troposphere. Furthermore, clouds are the principal modulator of this heating (Cox, 1969a). The effectiveness of clouds as modulators of the radiative heating may be attributed to their ability to absorb and emit significant amounts of infrared radiation at nearly any level in the atmosphere. The infrared radiative effects of clouds have been studied observationally by Cox (1969b) and Platt (1973) and theoretically by Flemming (1973), Yamamoto et al, (1970), and Liou (1973),

During the Line Island Experiment (LIE), 1967, daily infrared soundings were made from Christmas (2N) and Palmyra (6N) Islands (Zipser and Taylor, 1968). These soundings were made at approximately 9:00 - 10:00 p.m. LST, using a Suomi-Kuhn net radiometer. The instantaneous infrared heating rates were determined for 50 mb layers from these measurements.

A total of twenty-three soundings were made at Palmyra for the period from March 24 - April 18. The heating at 250 mb, 350 mb and 500 mb is shown as a function of time for this period in Fig. 1 . An

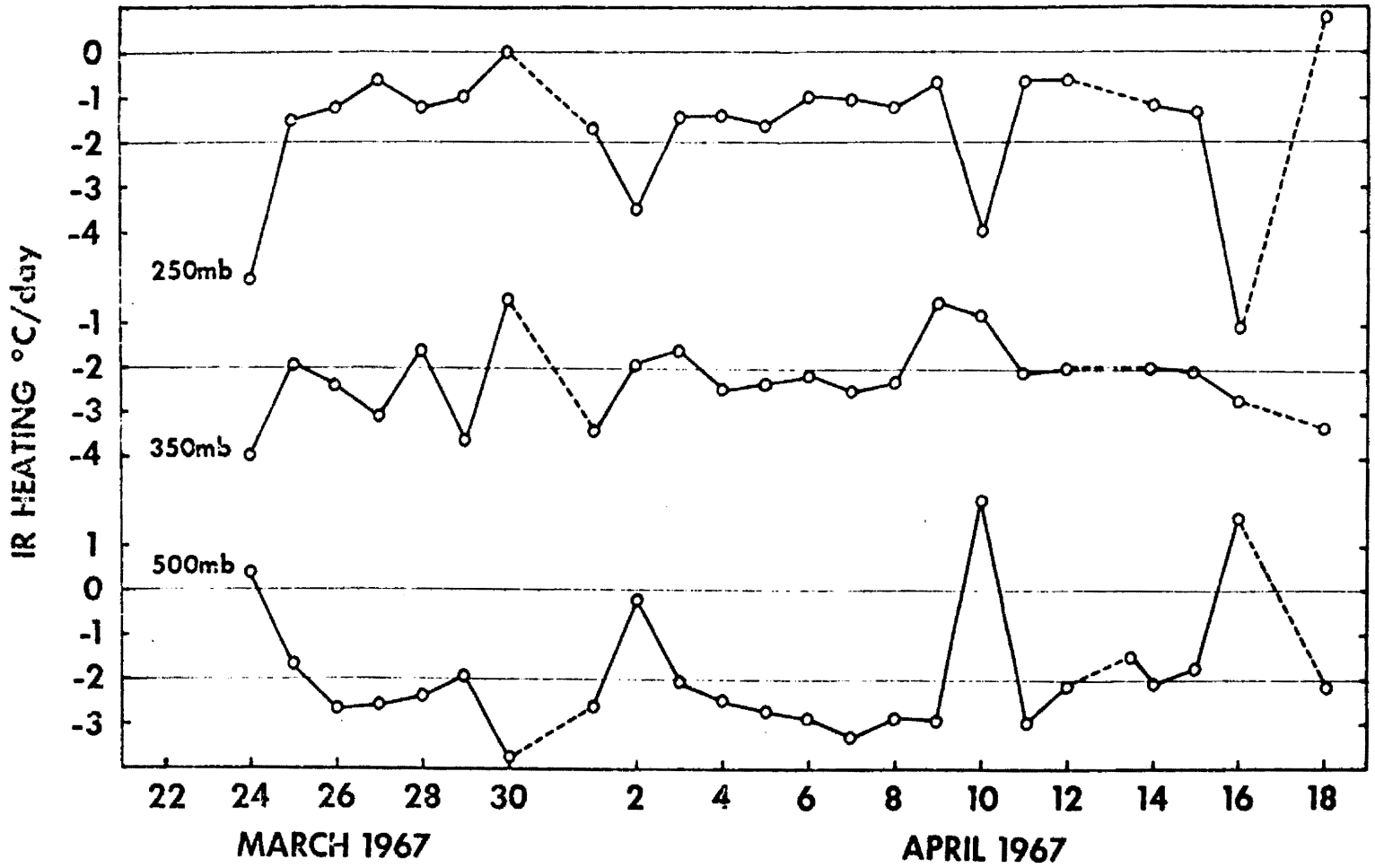

Figure 1. - Time series of infrared heating observed at Palmyra during the Line Island Experiment (1967).

interesting feature of the heating is the sharp increase in heating at 500 mb and the corresponding decrease at 250 mb occurring every six to eight days. The correlation coefficient calculated between the heating at 250 mb and 500 mb has the value of -.90 (Fig. 2). The heating in the 350 mb layer as shown by Fig. 1 and Fig. 2 shows little correlation with either the 250 mb or 500 mb level.

The average infrared heating for the four perturbed days indicated in Fig. 1 (March 24, April 2, 10, 16) is shown in Fig. 3 as a function of pressure. A significant feature of this heating profile is the large cooling in the 250-300 mb layer. The average magnitude of this cooling is nearly -5^{o} C day^{-1}. Equally significant is the warming of 1^{o} C day^{-1} at 500 mb.

There is little variation in the individual soundings making up the average infrared heating for the perturbed days. The upper tropospheric minimum ranges in height from 275 mb to 325 mb. The amplitude of this minimum ranged from -6.4 to -3.9^{o} C day^{-1}. The maximum middle tropospheric warming ranges in height from 525 mb - 625 mb and has an amplitude of .25 to 2.0^{o} C day^{-1}.

Figure 4 is an average of the infrared heating for the non-perturbed days. This profile shows little resemblance to that of the perturbed cases. This average profile shows a nearly constant heating of -2^{o} C day^{-1} below 450 mb. Above this level, the heating increases nearly linearly with pressure to a maximum of $.5^{o}$ C day^{-1} at 175 mb.

Upper tropospheric clouds appear to be responsible for the infrared heating which occurs on the perturbed days. Cox (1969a) has discussed the radiative effects of this type of cloud configuration. The effect of the clouds is made apparent by comparing the upward and downward longwave irradiance of the perturbed and the unperturbed cases as shown

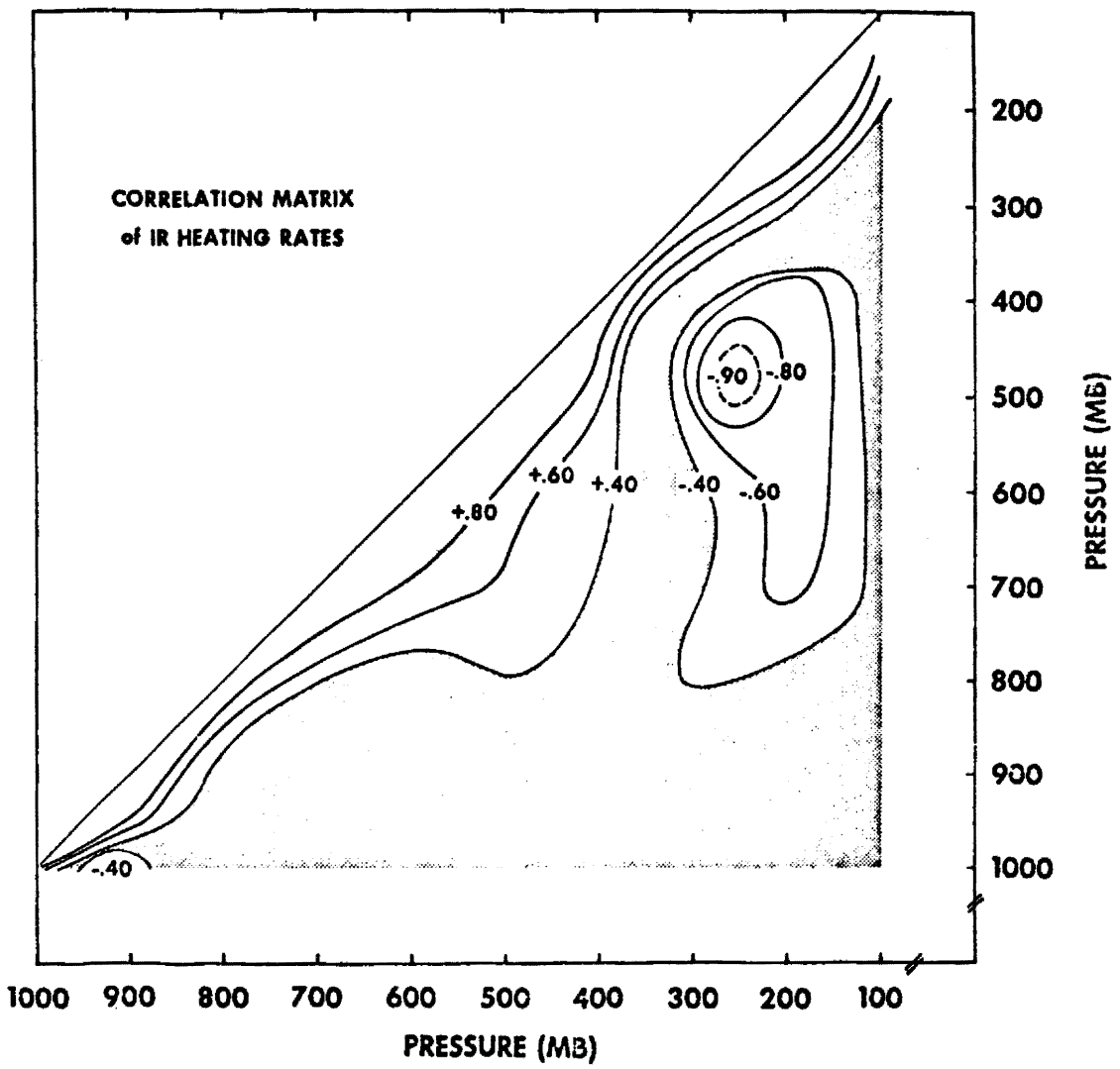

Figure 2. - Graphical depiction of correlation coefficients of infrared heating.

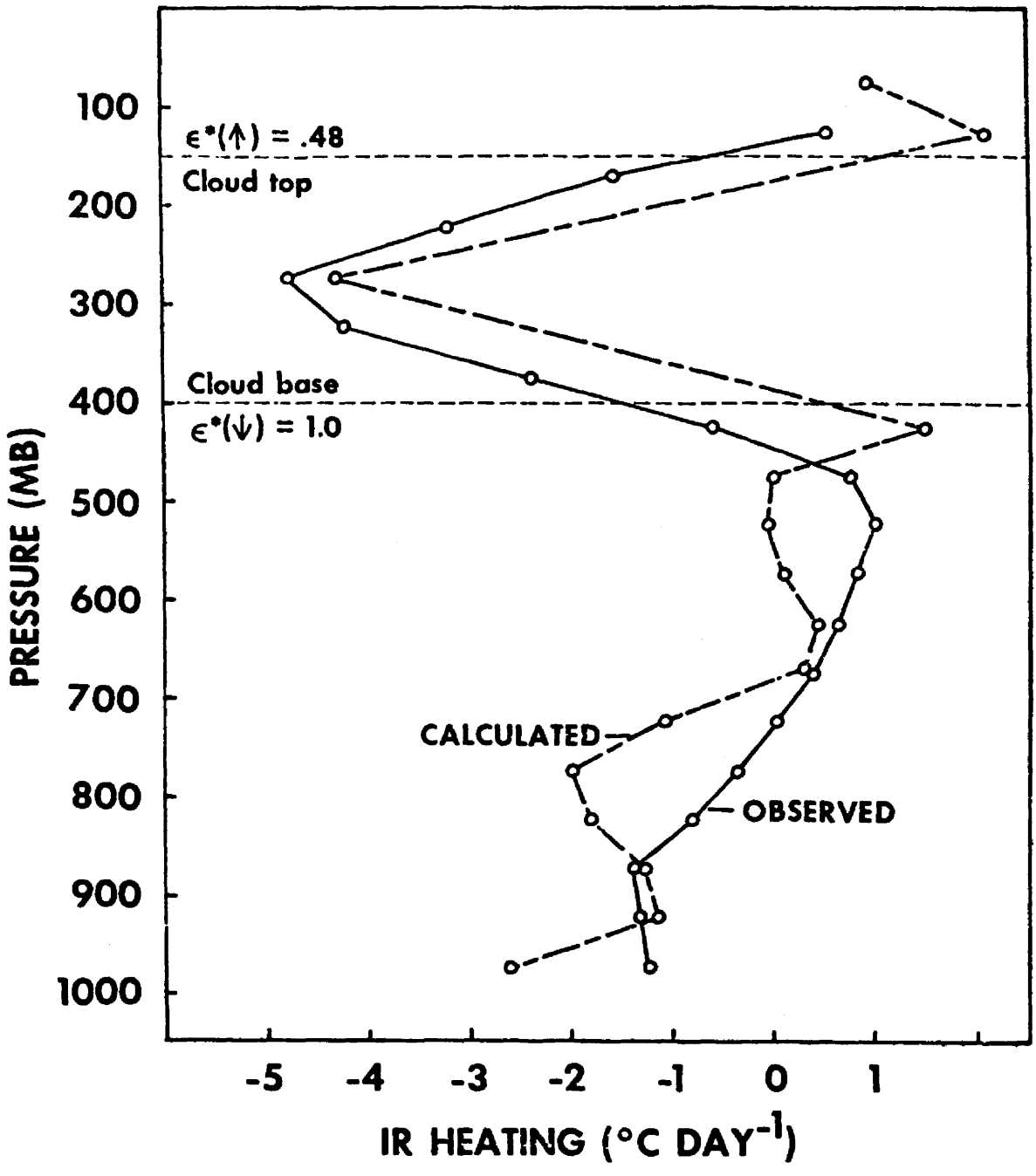

Figure 3. - Observed and calculated infrared heating profiles for perturbed days (March 24, April 2, 10, 16).

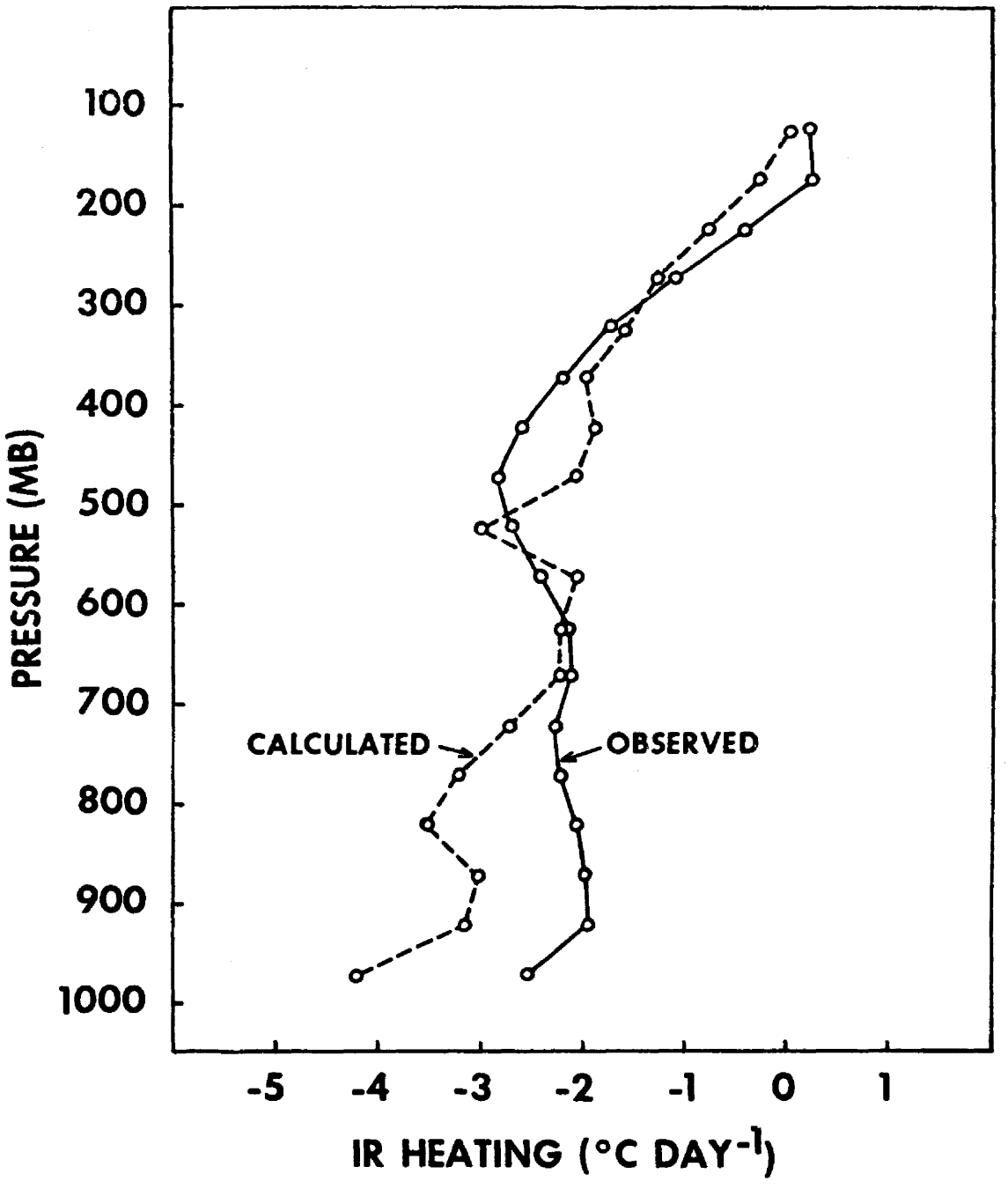

Figure 4. - Observed and calculated infrared heating profiles for unperturbed days (March 26, April 4, 6, 7, 8, 12, 14, 28).

in Fig. 5. From this representation, it is evident that the upward irradiance above 300 mb appears to converge with the downward irradiance below 450 mb. This convergence indicates the presence of some type of radiating element. Only water droplets or ice particles (clouds) could produce radiative effects of this magnitude. Saturation of the layer between 400 mb and 150 mb could change the heating by only $.25^{o}$ C day^{-1}.

It is difficult to determine the exact nature of the clouds in question from the average irradiance profiles. An examination of the individual soundings indicates that the clouds are at slightly different levels on different days causing a smoothing of the mean profile. Certain general features, however, are evident from the averaged profiles. From Fig. 5, it is apparent that the downward irradiance for the cloud case diverges from the non-perturbed case below 100 mb. This would indicate the presence of clouds near these levels. Likewise, the upward irradiance for the two cases diverges slowly above 600 mb and more rapidly above 400 mb, indicating the presence of clouds with bases in the middle troposphere.

Since the soundings were made at night, the cloud observations made from the surface may not give reliable information about the cloud structure at the time of the soundings. Surface observations made during the day indicate the presence of altocumulus, cirrus and cirrostratus. Satellite photographs also indicate significant areas of cloudiness in the vicinity of Palmyra for periods before and after the perturbed infrared heating profiles.

The presence of clouds is also evident in the moisture field. Figure 6 depicts the temperature and moisture profiles for the non-perturbed soundings and those for the perturbed case. The temperature

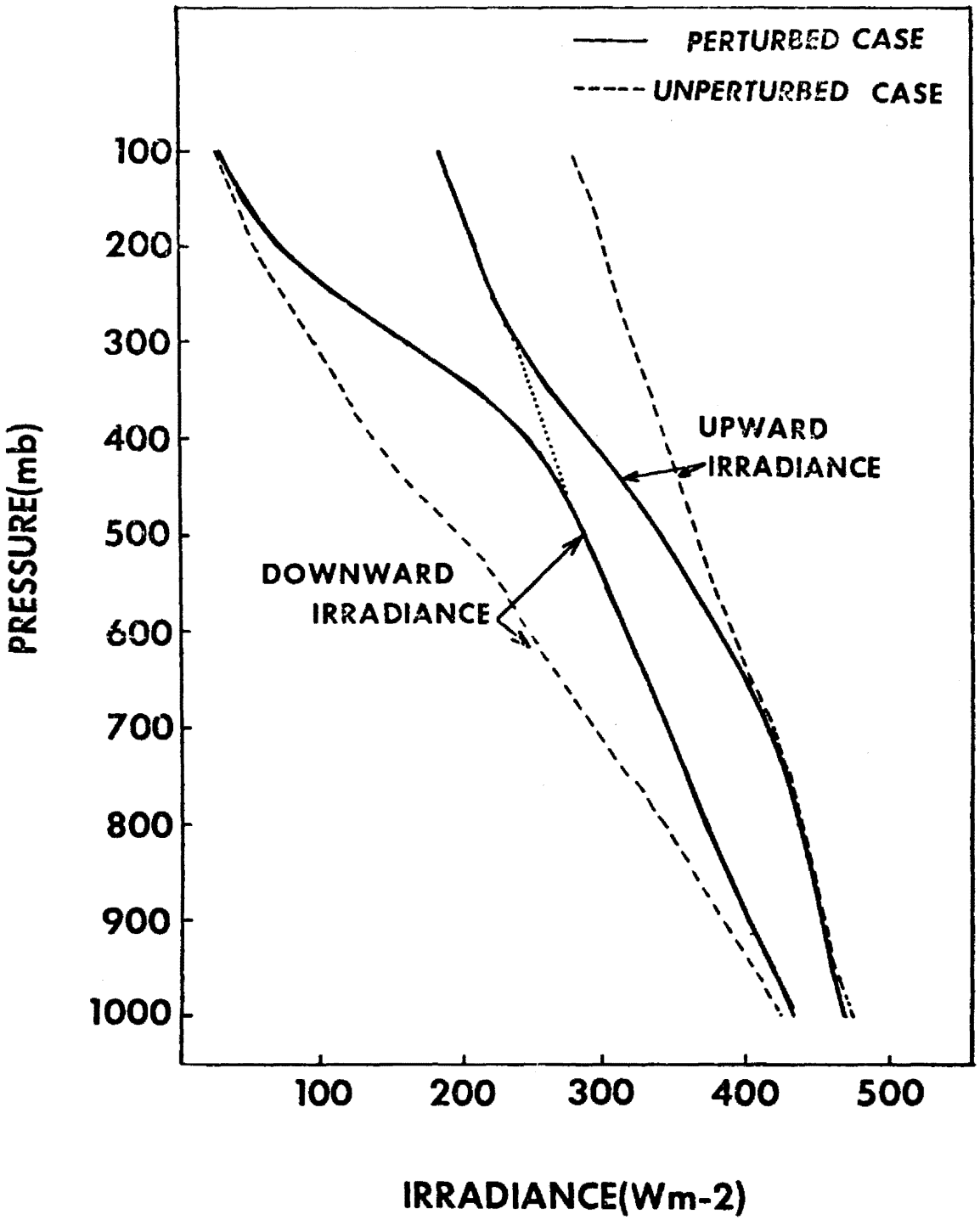

Figure 5. - Upward and downward infrared irradiance for the perturbed and unperturbed cases.

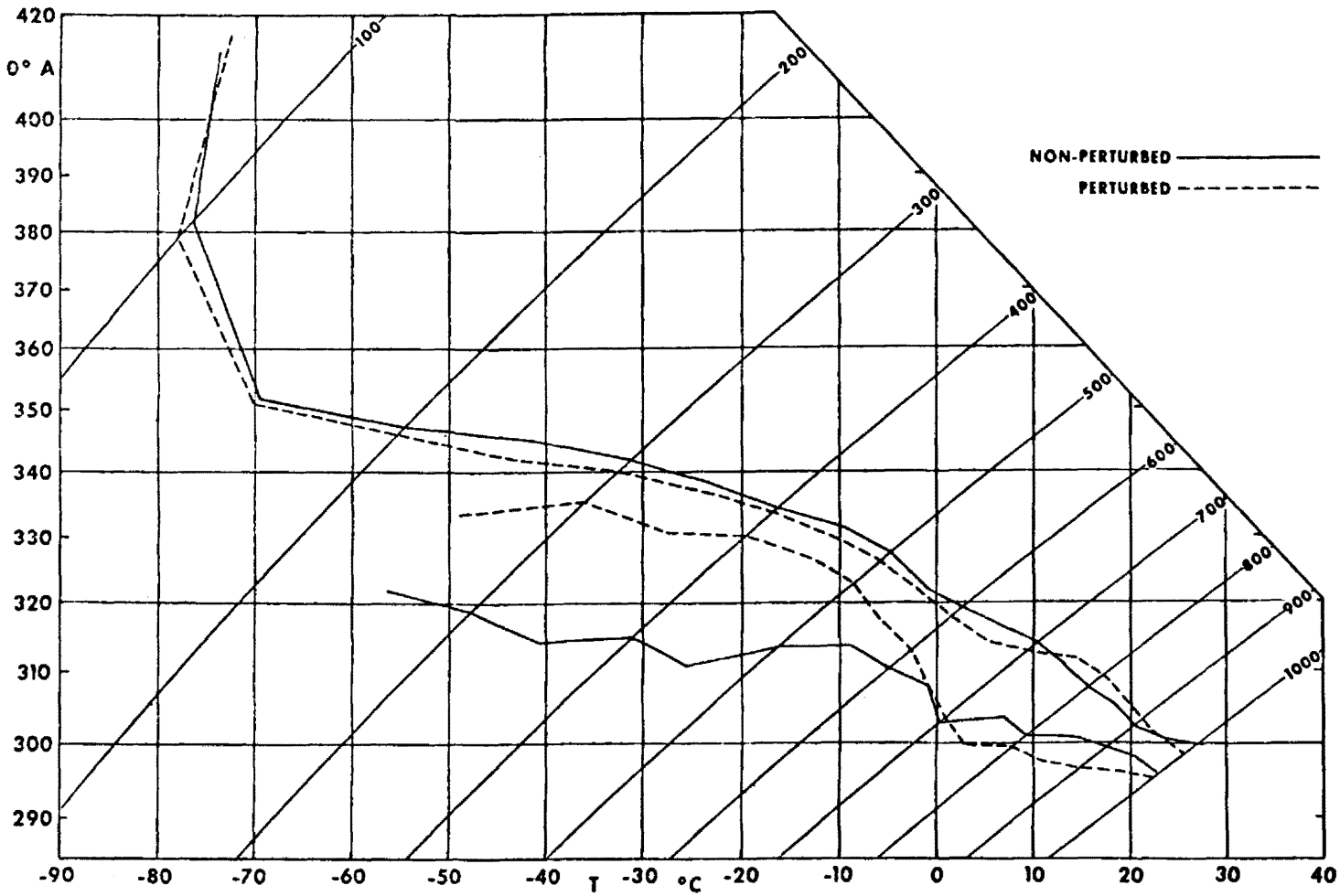

Figure 6. - Temperature and moisture profiles for the perturbed and unperturbed cases.

and moisture profiles were determined from radiosonde measurements made at night in conjunction with the radiometer ascents; hence, these measurements should not suffer from errors induced by solar radiation. The temperature profiles for the upper level cloud case are slightly cooler above 700 mb and slightly warmer below this level.

Although the temperature differences are small for the cloud case and the unperturbed case, there are significant differences in the moisture profiles. Above 500 mb, the relative humidity is considerably greater than for the undisturbed case. The region below 700 mb, however, is noticably drier.

From the description above, some estimates of the physical nature of the perturbed case cloud may be made. First it appears that cirrus and cirrostratus are present in the upper troposphere. These cirrus may tend to be rather deep with the possibility that there may be several layers. Secondly, since the base of the clouds may extend to 450 mb, water droplet clouds are likely to be present below the cirrus layers.

To gain further insight into how the radiation variations described above are manifested, the infrared heating was calculated using a long-wave transfer model described by Cox (1973). Clouds were included in the model using a technique outlined by Flemming (1973).

Temperature, moisture, and ozone concentration profiles were needed as input parameters for the model. For this purpose, the average temperature and moisture profiles shown in Fig. 6 were used. At heights where the observed parameters were not available, the temperature and humidity for 15^{o} N was taken from the United States Atmosphere Supplements (1966). The ozone profile was taken from an equatorial ozone model portrayed in the same publication.

If clouds are to be included in the model, the emissivity for the base and for the top of the cloud must be specified. Following a procedure outlined by Cox (1969a), the effective emissivity at the top of the cloud and that at the bottom are specified respectively as

$$\varepsilon^*(\uparrow) = \frac{H_T(\uparrow) - H_B(\uparrow)}{\sigma T^4_{CT} - H_B(\uparrow)} \tag{1}$$

and

$$\varepsilon^*(\downarrow) = \frac{H_B(\downarrow) - H_T(\downarrow)}{\sigma T^4_{CB} - H_T(\downarrow)} \tag{2}$$

where the $H_T(\uparrow)$ and $H_B(\uparrow)$ represent the upward irradiance at the top of the cloud and that at the base of the cloud. $H_T(\downarrow)$ and $H_B(\downarrow)$ are the downward irradiance at the top of the cloud and at its base. The temperature at the cloud base and cloud top are T_{CT} and T_{CB} respectively. σ is the Stefan-Boltzman constant.

If the top of the average disturbed case cloud is defined as 150 mb. and the base as 400 mb, $\varepsilon^*(\downarrow) = 1.0$ and $\varepsilon^*(\uparrow) = .48$. The results of the transfer calculation for this cloud are shown in Fig. 3. There is good agreement between the calculated and observed profiles. Slight improvement might be made by redefining cloud top and base. The calculated heating for the undisturbed case (Fig. 4) also exhibits good agreement with the observed profile. The deviations in the lower levels may be due to the presence of shallow clouds in the region of the trade inversion.

In the large-scale model, horizontal differences in the raidative heating are represented by the difference between the perturbed and unperturbed heating profile. Physically this represents horizontal differences in the upper tropospheric cloudiness.

There appears to be an organized distribution of clouds in the tropics. This fact is dramatically shown by time-longitude cross sections of satellite photographs (Chang, 1970; and Wallace, 1972). An example of this method of depicting the tropical cloudiness is shown in Fig. 7. From this representation of the clouds, it is apparent that the cloud systems move westward with time. These organized cloud patterns have a period of four to five days and a longitudinal separation of 2000-4000 km.

It is generally accepted that the organized tropical cloudy regions as seen from the satellite consist mostly of cirrus and cirrostratus clouds. Based on these observations, the infrared heating difference used in the model was assumed to have a period of five days and a longitudinal wavelength of 4,000 km.

B. Convective Heating

A determination of the convective heating from observations is generally not possible without radiation measurements. Furthermore, the convective heating may be quite variable in the vertical, depending on the height distribution of the clouds. This heating is also sensitive to variations in the large-scale motion field. A complete treatment of this problem would require a scheme such as that proposed by Arakawa and Schubert (1974). In the diagnostic model, no consideration is given to the complex interaction between the heating and the large-scale motion field.

Since the model requires that the heating be specified, an average value of the convective heating must be used. Although the specification of this heating may be somewhat arbitrary, we have chosen to make use of the apparent heat source of a region in the western Pacific as determined by Yanai et al.(1973).

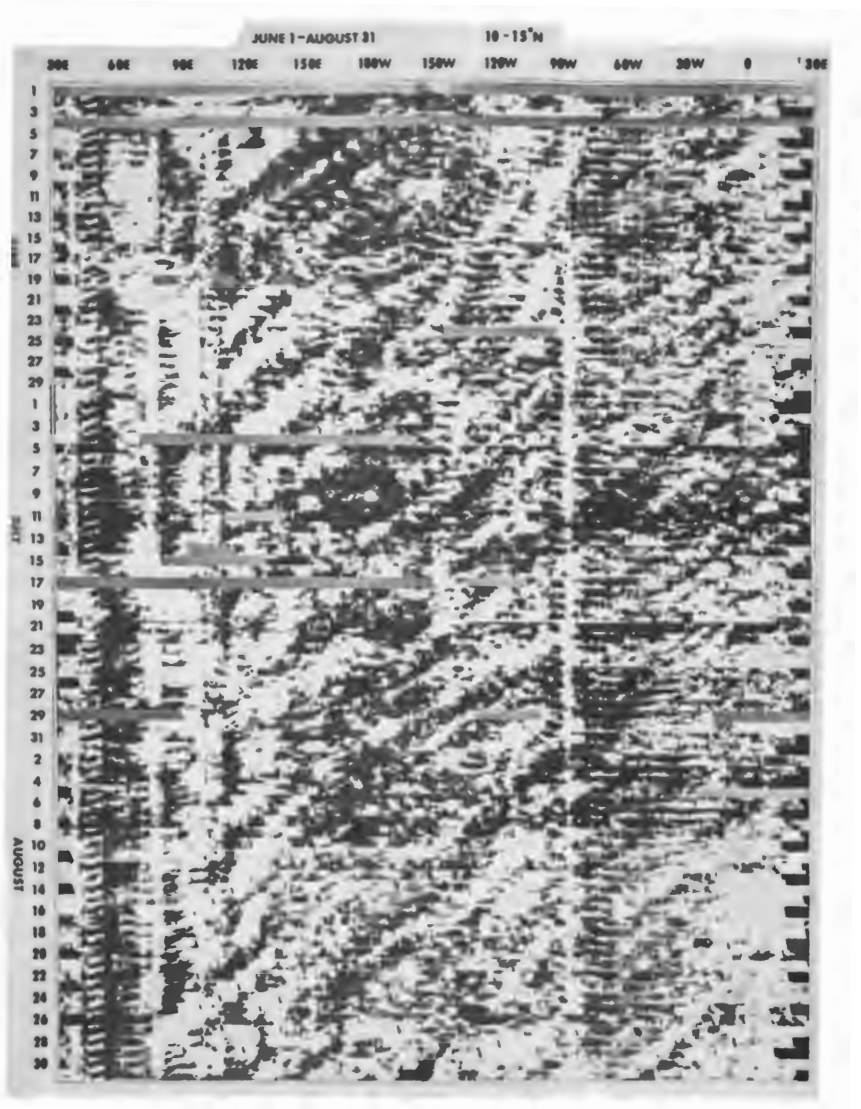

Figure 7. - Time-longitude section of satellite determined tropical cloudiness (after Wallace, 1971).

This apparent heat source consists of the convective and radiative heating. This heating, called Q_1 by Yanai et al.(1973), has the vertical distribution shown in Fig. 8. If it is assumed that the area investigated by Yanai included both perturbed and unperturbed radiation cases, the radiative heating included in Q_1 may be approximated by some mean value. The mean infrared heating (Q_{RM}) for 15^{o} N, summer (Cox, 1969a) is assumed to be the mean infrared heating term in Q_1.

The convective heating for the area may then be deduced by subtracting the average infrared heating (Q_{RM}) from the apparent heat source, Q_1. This quantity (Q_1-Q_{RM}) is shown in Fig. 8. It has approximately the same vertical distribution as Q_1, with the maximum at 6 km increased by approximately 2^{o} C day^{-1}.

(Q_1-C_{RM}) is used in the model to represent the difference in convective heating between areas of strong convection and those with little convection.

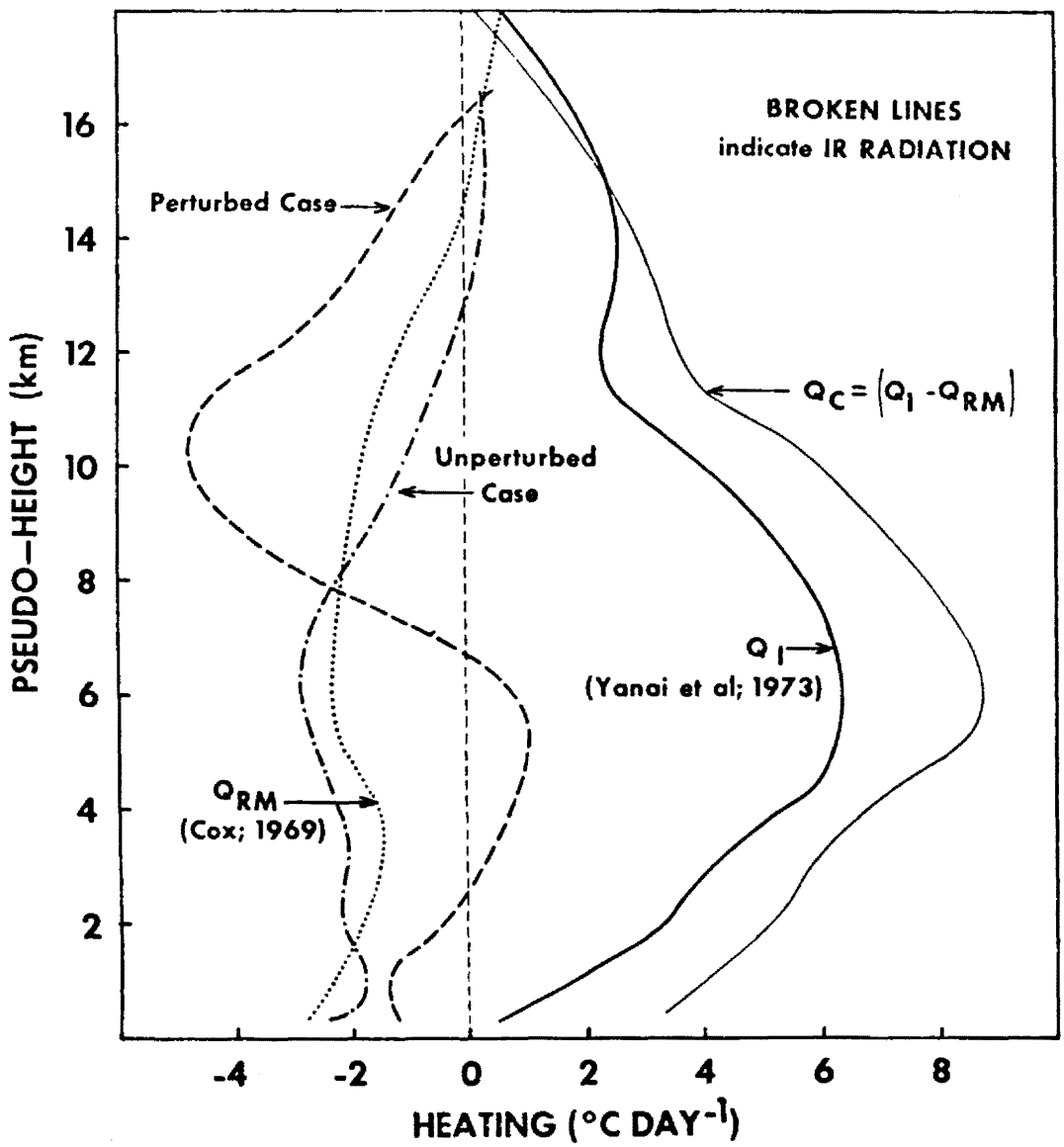

Figure 8. - Vertical profiles of apparent heat source, (Q_1), mean infrared radiation (Q_{RM}), difference between apparent heat source and mean radiation (Q_1-Q_{RM}), and infrared heating for perturbed and unperturbed cases.

III. LARGE-SCALE DIAGNOSTIC MODEL

A large-scale model will be used to determine the response of the atmosphere to various convective and infrared heat sources. This model is nearly identical to the model formulated by Holton (1971). The diabatic heating is specified and the resulting motions forced by the heating are determined.

In this model, the horizontal momentum equations, the hydrostatic equation, the continuity equation, and the thermodynamic equation are combined into a single second order partial differential equation. This equation has variable coefficients and is solved numerically to obtain the geopotential height variations resulting from a specified heating distribution. The remaining variables are determined from this geopotential height field.

A. Description of the Model

The independent variables used in the model are (λ, ϕ, ξ), where λ is the longitude, ϕ is the latitude, and ξ is the vertical coordinate defined by

$$\xi = - H \ln \frac{p}{p_o} ,$$

where H is a constant vertical scale height, p is the pressure, and p_o is a sea level reference pressure.

The pseudo-height, ξ, is related to the actual height, z, through the hydrostatic relationship,

$$\frac{d\xi}{H} = \frac{g\, dz}{RT} \qquad (3)$$

where T is the temperature at height z and pressure p. Figure 9 is a graphical representation of the relationship between the three vertical

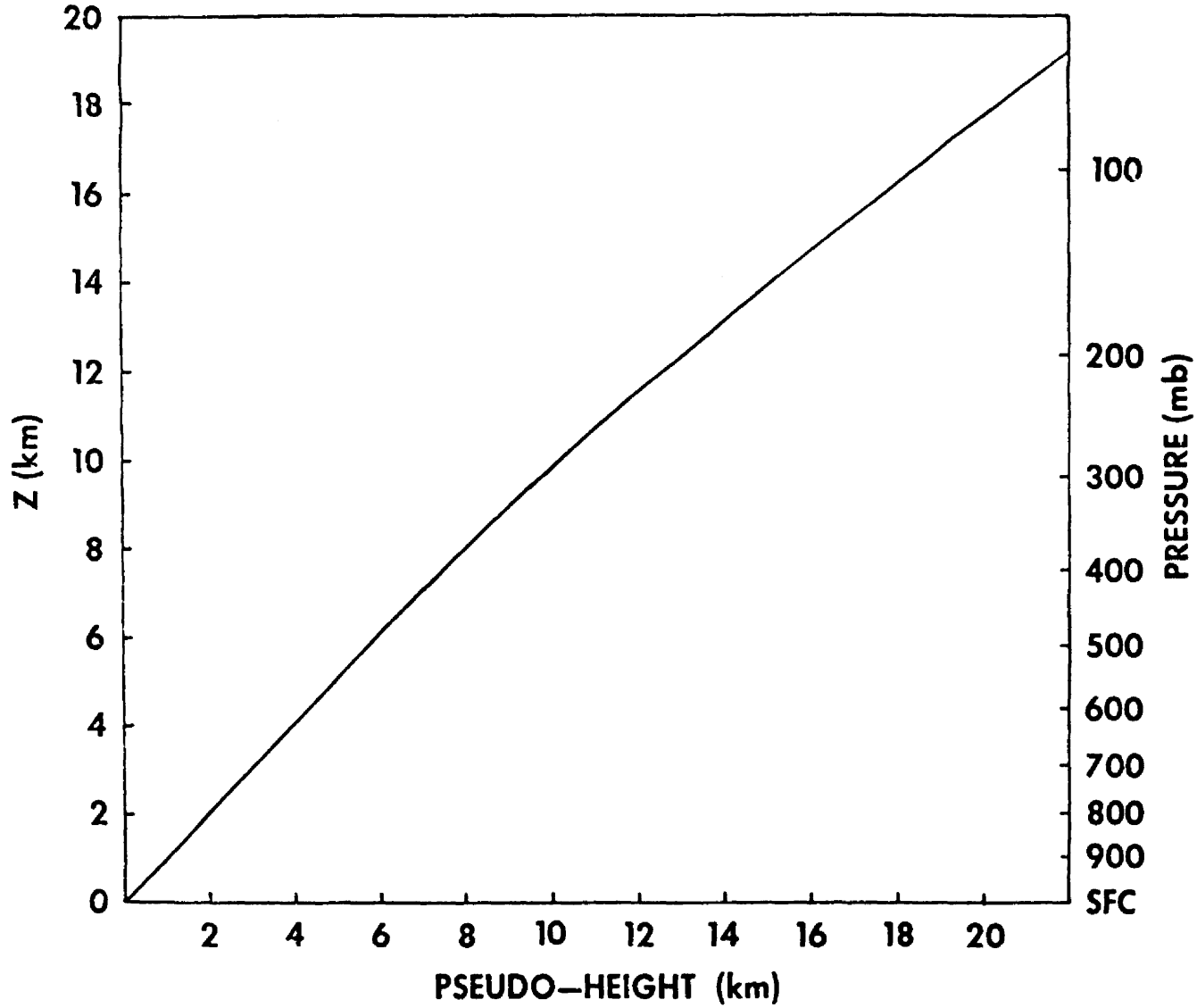

Figure 9. - Graphical representation of relationship between pressure, (p), pseudo-height, (ξ), and actual height, (z).

variables, ξ , z, and p. This graph was constructed using the temperature structure for a typical tropical atmosphere, with H = 8 km. There is little difference between ξ and z below heights of 10 km and only a 10% difference at z = 18 km. In the psuedo-height system, the vertical velocity is defined as $w = \frac{d\xi}{dt}$.

In linearized form (see Appendix A), the horizontal momentum equations, the hydrostatic equation, the continuity equation and the first law of thermodynamics may be written as

$$\frac{\partial u}{\partial t} + \frac{\bar{u}}{a \cos\phi}\frac{\partial u}{\partial \lambda} - \frac{v\bar{u}}{a}\tan\phi + \frac{v}{a}\frac{\partial \bar{u}}{\partial \phi} = - \frac{\partial \Phi}{a \cos\phi \, \partial\lambda} + 2\Omega v \sin\phi - \kappa u , \tag{4}$$

$$\frac{\partial v}{\partial t} + \frac{\bar{u}}{a \cos\phi}\frac{\partial v}{\partial \lambda} + \frac{2u\bar{u}}{a}\tan\phi = - \frac{\partial \Phi}{a\partial\phi} - 2\Omega u \sin\phi - \kappa v, \tag{5}$$

$$\frac{\partial \Phi}{\partial \xi} = \frac{RT}{H} , \tag{6}$$

$$\frac{1}{a\cos\phi}\frac{\partial u}{\partial \lambda} + \frac{1}{a}\frac{\partial v}{\partial \phi} - \frac{v}{a}\tan\phi + e^{\xi/H}\frac{\partial}{\partial \xi}(e^{-\xi/H}w) = 0, \tag{7}$$

$$\frac{\partial T}{\partial t} + \frac{\bar{u}}{a\cos\phi}\frac{\partial T}{\partial \lambda} + w\left(\frac{R\bar{T}}{C_p H} + \frac{d\bar{T}}{d\xi}\right) = \frac{Q}{C_p} - \kappa T , \tag{8}$$

where the terms $w\frac{\partial \bar{u}}{\partial \xi}$ and $\frac{v}{a}\frac{\partial \bar{T}}{\partial \phi}$ have been neglected and may be shown 'a posteriori' to be small compared to the other terms. In Eqs. (4) - (8), u, v, and w represent the zonal, meridional, and vertical velocity perturbations. Φ is the geopotential height perturbation and $\bar{u}$ and $\bar{T}$ are the time-zonally averaged zonal velocity and temperature fields. Q represents the diabatic heating per unit mass due to horizontal differences in radiation and convection, and C_p is the specific heat of air at constant pressure. In Eq. (4) and (5), κ is the Rayleigh drag coefficient and in Eq. (8), it represents a rate coefficient for Newtonian cooling.

Following the procedure outlined by Holton (1971), Eq. (4) - (8) are expressed in nondimensional form. The horizontal scale dimension is defined as the radius of the earth, a. The vertical scale dimension is defined as the scale height, H, and the reciprocal of twice the earth's angular velocity, $(2\Omega)^{-1}$, is specified as the time scale dimension. Using these scale dimensions, a set of nondimensional variables may be defined as

$$\left.\begin{aligned} u^* &= u \cos\phi \, (2\Omega a)^{-1} \\ v^* &= v \cos\phi \, (2\Omega a)^{-1} \\ \bar{u}^* &= \bar{u} \cos\phi \, (2\Omega a)^{-1} \\ w^* &= w \, (2\Omega H)^{-1} \\ \Phi^* &= \Phi \, (2\Omega a)^{-2} \\ T^* &= RT(2\Omega a)^{-2} \\ \bar{T}^* &= R\bar{T}(2\Omega a)^{-2} \\ Q^* &= RQ(2\Omega a)^{-2} \, (2\Omega C_p)^{-1} \end{aligned}\right\} . \qquad (9)$$

With the aid of Eq. (9) and defining $y \equiv \sin\phi$, Eqs. (4) - (8) may be written as

$$\frac{\partial u^*}{\partial t^*} + \frac{\bar{u}^*}{1-y^2} \frac{\partial u^*}{\partial \lambda} + \left(\frac{\partial u^*}{\partial y} - y\right) v^* = - \frac{\partial \phi^*}{\partial \lambda} - Du^* , \qquad (10)$$

$$\frac{\partial v^*}{\partial t^*} + \frac{\bar{u}}{1-y^2} \frac{\partial v^*}{\partial \lambda} + \left(\frac{2\bar{u}^*}{1-y^2} + 1\right) yu^* = - (1-y^2) \frac{\partial \phi^*}{\partial y} - Dv^* , \qquad (11)$$

$$\frac{\partial \phi^*}{\partial \xi^*} = T^* , \qquad (12)$$

$$\frac{1}{1-y^2} \frac{\partial u^*}{\partial \lambda} + \frac{\partial v^*}{\partial y} + e^{\xi^*} \frac{\partial}{\partial \xi^*} (e^{-\xi^*} w) = 0, \qquad (13)$$

$$\frac{\partial T^*}{\partial t^*} + \frac{\bar{u}^*}{1-y^2} \frac{\partial T^*}{\partial \lambda} + w^* S = Q^* - DT , \qquad (14)$$

where $\xi^* = \frac{\xi}{H}$, $t^* = t(2\Omega)$ and $D \equiv \kappa(2\Omega)^{-1}$ is a dimensionless dissipation coefficient. $S = \frac{R\bar{T}^*}{C_p} + \frac{d\bar{T}^*}{d\xi^*}$ is the dimensionless static stability parameter.

If the heating has a temporal and longitudinal variation of the form

$$Q^* = Q'(y, \xi^*) \exp[i(k\lambda + \omega t^*) + \frac{\xi^*}{2}] \tag{15a}$$

where k is the zonal wave number and ω is the frequency of the westward propogating heat sources, the dependent variables will be forced to have the form

$$\left.\begin{aligned} u^* &= u'(y, \xi^*) \\ v^* &= v'(y, \xi^*) \\ w^* &= w'(y, \xi^*) \\ \Phi^* &= \Phi'(y, \xi^*) \\ T^* &= T'(y, \xi^*) \end{aligned}\right\} \exp[i(k\lambda + \omega t^*) + \frac{\xi^*}{2}] \tag{15b}$$

where the primed quantities may be complex. Using Eq. (15), Eqs. (10) - (14) may be written as

$$i\,\hat{\omega}\,u' + (\frac{\partial \bar{u}^*}{\partial y} - y)\,v' = -i\,k\,\Phi' , \tag{16}$$

$$i\,\hat{\omega}\,v' + (\frac{2y\bar{u}^*}{(1-y^2)} + y)\,u' = -(1-y^2)\,\frac{\partial \Phi}{\partial y} , \tag{17}$$

$$(\frac{\partial}{\partial \xi^*} + \frac{1}{2})\,\Phi = T' , \tag{18}$$

$$\frac{iku'}{(1-y^2)} + \frac{\partial v'}{\partial y} + (\frac{\partial}{\partial \xi^*} - \frac{1}{2})\,w' , \tag{19}$$

$$i\,\hat{\omega}\,T' + w'\,S = Q' , \tag{20}$$

where

$$\hat{\omega} = \omega + \frac{k\bar{u}}{1-y^2} - iD$$

Holton (1971) assumes that the mean zonal wind has a latitudinal variation of the form $\bar{u}^* = u_o(\xi^*)\,(1-y^2)$. Assuming this variation reduces Eqs. (16) and (17) to

$$i\,\hat{\omega}\,u' - (2u_0 + 1)\,yv' = -i\,k\,\Phi' \,, \tag{16a}$$

and

$$i\,\hat{\omega}\,v' + (2u_0 + 1)\,yu' = -(1-y^2)\,\frac{\partial \Phi'}{\partial y} \,. \tag{17a}$$

If the mean zonal wind is assumed to be approximately 10 m sec^{-1}, the nondimensional $u_0(\xi)$ will be approximately .01. Hence, the terms involving u_0 in Eqs. (16a) and (17a) may be ignored. Making this approximation, Eqs. (16a) and (17a) may be used to express v' and u' as

$$u' = \frac{\hat{\omega}\,k\,\Phi' - y(1-y^2)\,\frac{\partial \Phi'}{\partial y}}{y^2 - \hat{\omega}^2} \,, \tag{21}$$

$$v' = \frac{i\,k\,y\,\Phi' - i\,\hat{\omega}(1-y^2)\,\frac{\partial \Phi'}{\partial y}}{y^2 - \hat{\omega}^2} \tag{22}$$

Using Eq. (18) to eliminate the temperature from Eq. (20) we obtain

$$i\,\hat{\omega}\left(\frac{\partial}{\partial \xi^*} + \frac{1}{2}\right)\Phi' + w'S = Q' \tag{23}$$

Equations (19), (21), (22) and (23) form a set of four equations and four unknowns. The variables u', v' and w' may be eliminated from these equations to form the single partial differential equation

$$\frac{\partial^2 \Phi'}{\partial \xi^{*2}} - \sigma\,\frac{\partial \Phi'}{\partial \xi^*} + S\,\frac{\partial}{\partial y}\left[\frac{(1-y^2)}{(y^2 - \hat{\omega}^2)}\,\frac{\partial \Phi'}{\partial y}\right] + \tag{24}$$

$$\left[\frac{S}{(y^2-\omega^2)}\left(\frac{k}{\hat{\omega}}\,\frac{(y^2 + \hat{\omega}^2)}{(y^2 - \hat{\omega}^2)} - \frac{k}{1-y^2}\right) - \left(\frac{1}{4} + \frac{\sigma}{2}\right)\right]\Phi' = \frac{iS}{\hat{\omega}}\left(\frac{\partial}{\partial \xi^*} - \frac{1}{2}\right)\frac{Q'}{S} \,,$$

where $\sigma \equiv -\frac{S}{\hat{\omega}}\,\frac{d}{d\xi^*}\left(\frac{\hat{\omega}}{S}\right)$. This equation is identical to the differential equation derived by Holton (1971).

Since $\hat{\omega}$ is a function of ξ, this differential equation must be solved numerically. The solution to an equation of this form has been outlined by Lindzen and Kuo (1969) and is described in detail in Appendix B.

B. Boundary Conditions and Specification of Parameters

To obtain solutions to the partial differential Eq. (24), it is necessary to specify a y - ξ grid and appropriate boundary conditions. In the cases studied in this paper, the vertical spacing of grid points was chosen as $\Delta\xi$ = 1 km and the horizontal spacing as Δy = .030 ($\sim 1.6^{o}$ latitude).

The northern boundary was placed at $\phi = 28.7^{o}$ N (y=.48). At this boundary the perturbation geopotential height was specified to be zero. This condition was also imposed at ϕ = 13.95 (y = -.24).

At the lower boundary vertical velocity is required to be zero. If there is no heating at the boundary, Eq. (20) implies that the temperature perturbations will also be zero at this boundary. The upper boundary was specified at ξ = 21 km. The geopotential height perturbations at this boundary were required to be zero. To determine the effect this rather restrictive condition might have on the response of the model, the boundary was specified two kilometers lower. Little effect on the response could be detected.

The parameters S, D, κ, ω, u_0 and Q need to be specified as known quantities in Eq. (24). The static stability parameter, S, was computed from a 100 day time average over Yanai's pentagon network (Yanai et al, 1973). The dimensional form of this stability is shown in Fig. (10). The stability decreases with height to a minimum at 12 km. It then increases with height above this level to 19 km, where the atmosphere becomes isothermal and the static stability is constant with height.

The dissipation, D, is considered to constant with height. The value of D chosen corresponds to a damping time of sixteen days, similar to the damping used by Holton (1972).

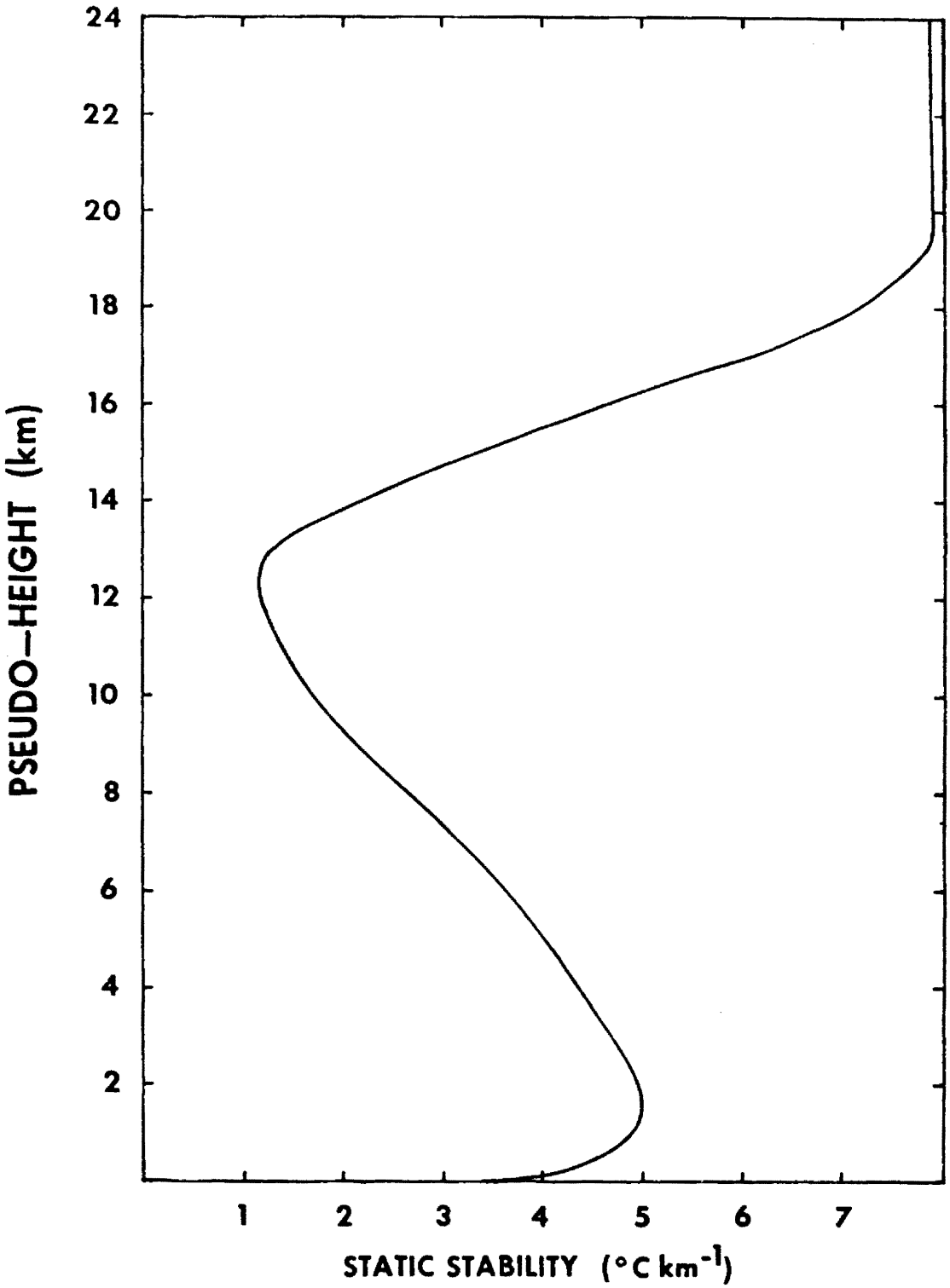

Figure 10. - Static stability used in the model.

The heating $Q'(y, \xi) \exp[i(k\lambda + \omega t^*) + \frac{\xi^*}{2}]$ is specified as an external parameter. For all the cases considered, the heating is assumed to have a wavelength of 4,000 km and a period of five days. The complex amplitude $Q'(y, z)$ is specified to have the same variation with latitude as that used by Holton (1971), i.e.

$$Q'(y, \xi) = Q_C(\xi) \exp[-\frac{(y-y_C)^2}{\alpha_C}] + Q_R(\xi) \exp[-\frac{(y-y_r)^2}{\alpha_r}] e^{i\theta}, \quad (25)$$

where Q_C in Eq. (25) represents the convective heating (i.e. $\frac{1}{2}$ of the difference between the heating at the ridge and the trough of the Q wave). Q_R is the corresponding diabatic heating due to horizontal gradients in the radiation field. Q_R will have the same zonal and temporal dependence as Q_C but with a phase difference of θ. The quantities y_C and y_r define the latitudes of maximum convective and radiative heating. The parameters α_C and α_r determine the meridional extent of the heating terms described above. In this study, $y_C = y_r = .15(\phi = 8.6^o\ N)$ and $\alpha_r = \alpha_C = .05$ corresponding to a half width of approximately 3^o latitude. The only parameters that need be specified are $Q_C(\xi)$, $Q_r(\xi)$, $u_o(\xi)$, and θ.

C. Verification of the Model

The solution of Eq. (24) is somewhat complicated to perform numerically. Consequently, several checks were made to insure that the solution was correct.

The usual method of checking the solution of a partial differential equation is to determine if the original differential equation and the boundary conditions are satisfied. The boundary conditions in this problem are relatively simple and are easily varified from the results. For the points within the boundaries, the geopotential height field

determined numerically from the differential equation (24) was substituted into the finite difference form of the left hand side of this equation. The result of this calculation was then compared to the right hand side of the equation. There was agreement to at least four significant figures in these two computations.

To further insure that the solution was correct, the static stability and the heating used by Holton (1971) were tested in the model. The northern boundary was placed at $\phi = 40^{o}$ N. The southern boundary was placed at the equator with the condition that the geopotential height be symmetric about the equator. The upper boundary was placed at $\xi = 19$ km and the temperature perturbations were required to be zero at $\xi = 0$.

Figure (11) is a meridional cross section of the amplitude of the meridional wind perturbation calculated using the parameters defined above. Figure (12) portrays the identical cross section as calculated by Holton (1971). There is excellent agreement between these two calculations. There is, however, a slight difference at the lower boundary. Although Holton does not explicitly define the lower boundary condition, it appears that the difference in the two calculations may result from differences in the treatment of the lower boundary. Similar agreement was found for the temperature and the vertical velocity perturbations.

To gain further insight into the ability of the model to simulate tropospheric waves, the results from the model were compared to the observed wave structure. This comparison was made by incorporating into the model the difference between the diabatic heating at the ridge and the trough of the waves as determined by Reed and Recker (1971). The structure of the wave forced by this heating is then compared to the structure observed by Reed and Recker (1971).

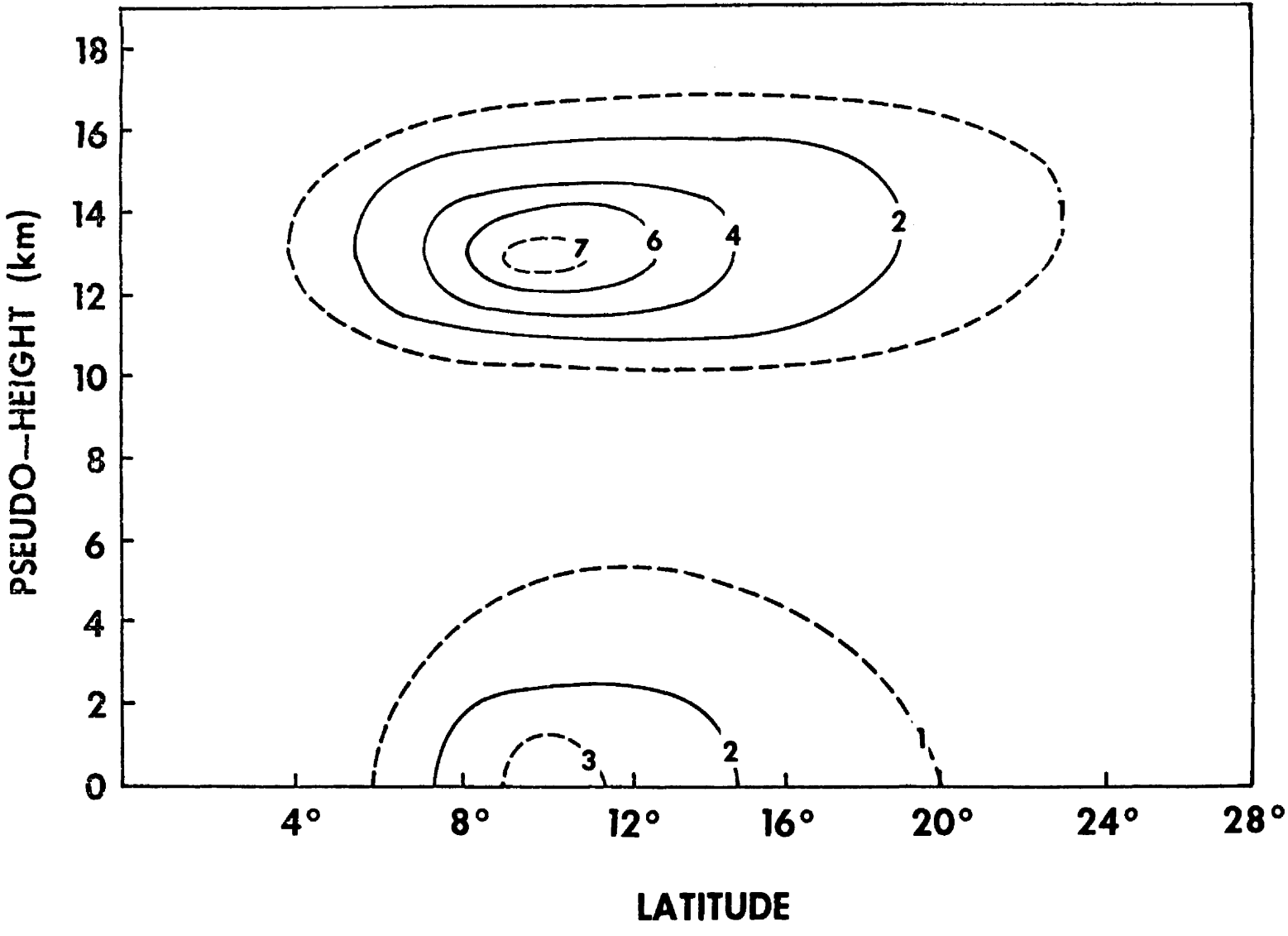

Figure 11. - Amplitude of meridional wind (m sec^{-1}) calculated using Holton's (1971) diabatic heating.

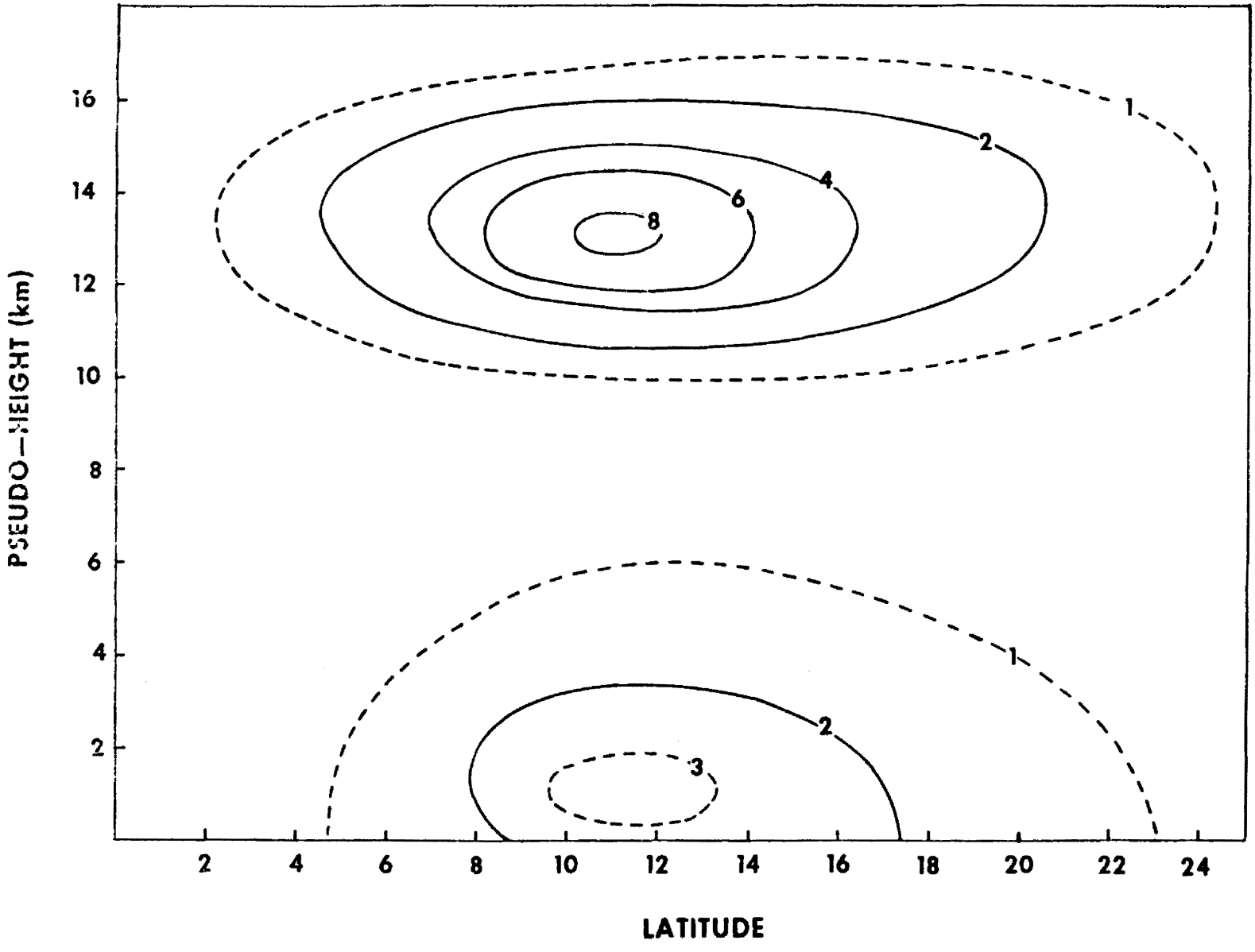

Figure 12. - Amplitude of meridional wind (m sec^{-1}) calculated by Holton (1971).

The vertical profile of the diabatic heating used in the model is shown in Fig. 13. This heating profile represents the difference between the large scale energy budget of the trough and ridge regions of the waves. Since the sinusoidally varying portion of $Q'(y, \xi)$ will range in value from -1 to +1, only one half of this heating was substituted for Q_c in the model. Hence, the difference in $Q'(y, \xi)$ across one half of its wavelength will be identical to the heating function specified by Reed and Recker. The heating was assumed to have a period of five days and wavelength of 4000 km.

The mean zonal wind reported by Reed and Recker (1971) for the KEP triangle (Fig. 14) was substituted in nondimensional form for $u_o(\xi)$. The calculated meridional wind perturbations are shown in Fig. 15. The abscissa of this cross section is presented in terms of longitude. It may also be interpreted as time with a period corresponding to five days. This meridional wind structure shows a weak cyclonic curvature in the lower troposphere. A stronger anticyclonic curvature is evident at 13 km with the maximum winds being 3 m sec^{-1}. In the middle levels, there is a slight eastward tilt with height; a westward tilt with height occurs above 16 km.

The observed meridional wind is shown in Fig. 16. The general features are similar to the calculated perturbations. The lower level disturbance, however, is significantly stronger than the calculated perturbations. Holton (1971) has suggested that some form of cooling in the lowest layers may be important to the energetics of this lower level circulation.

The calculated meridional wind perturbations are somewhat greater than the observed variations in the upper level circulation. Reed and

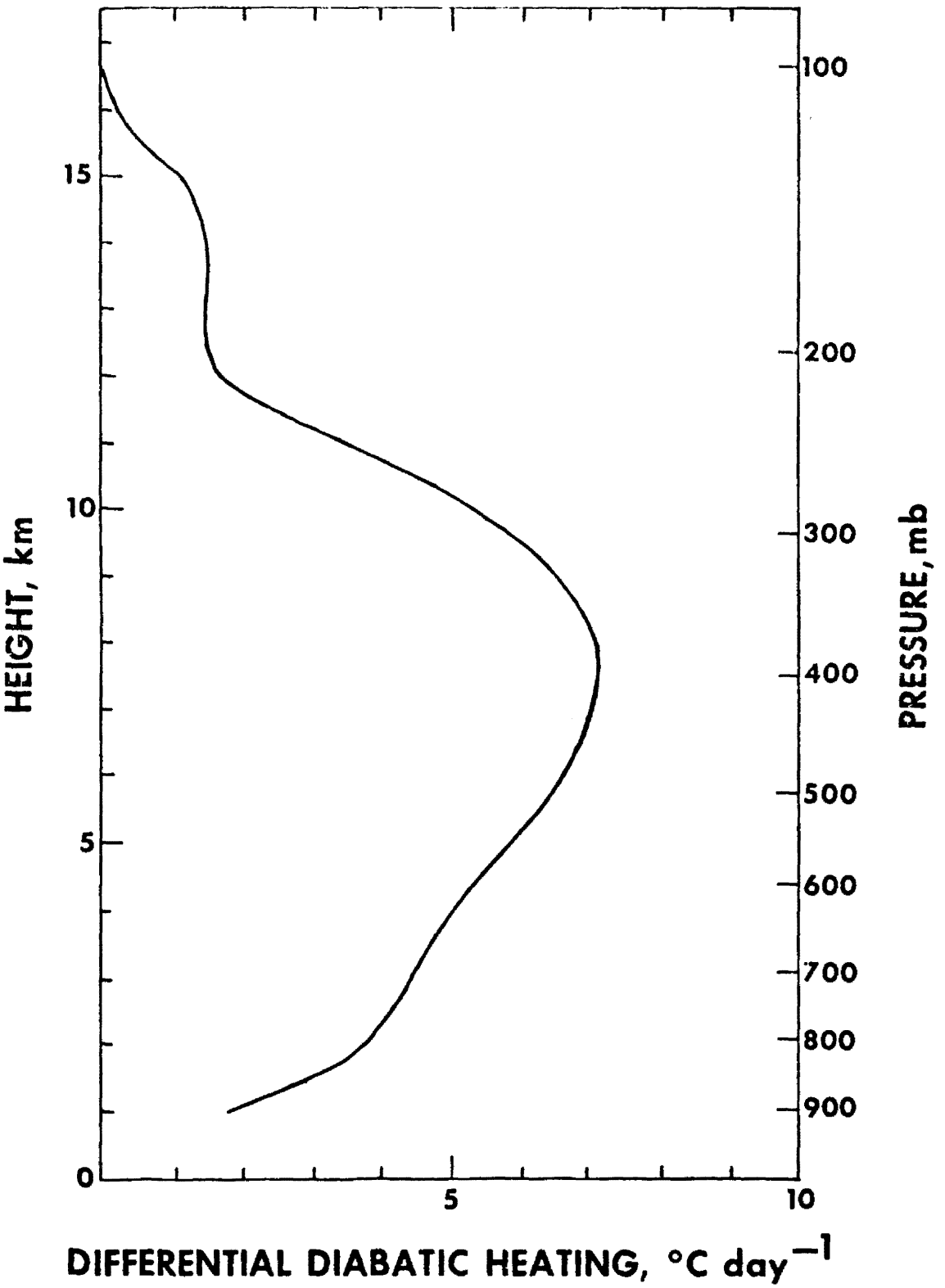

Figure 13. - The heating difference between the trough and ridge as determined by Reed and Recker (1971).

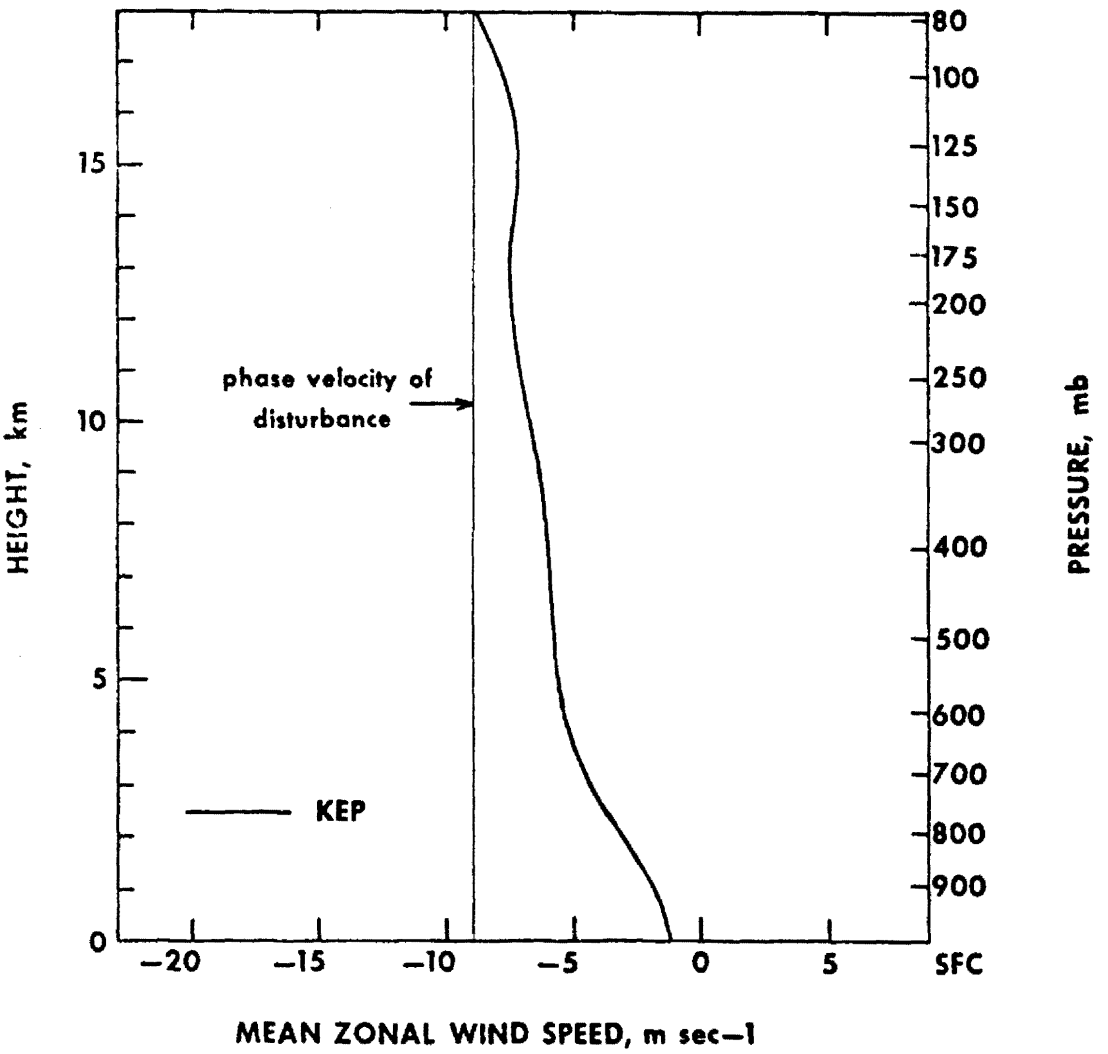

Figure 14. - Vertical profile of the mean zonal wind for KEP (after Reed and Recker, 1971).

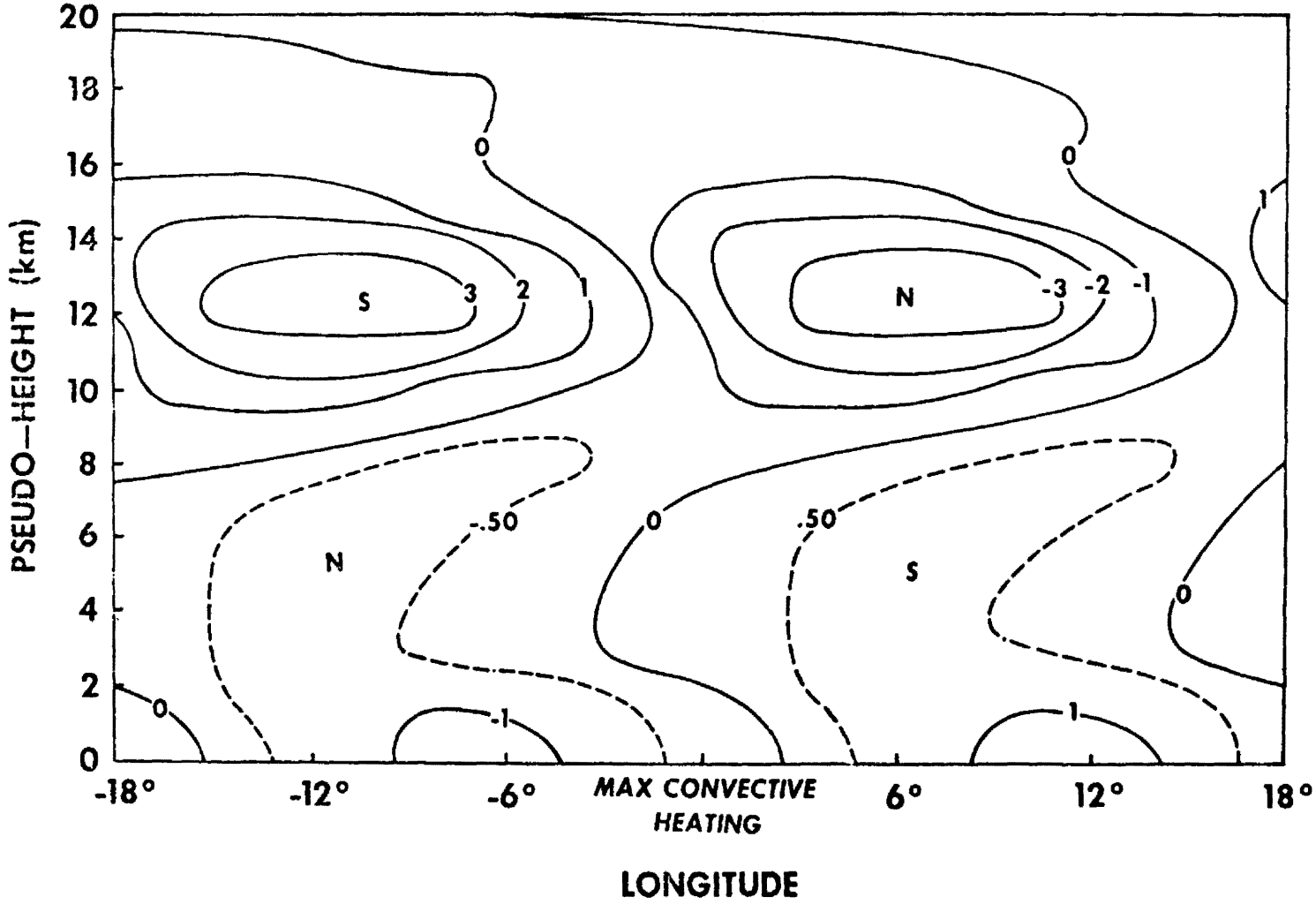

Figure 15. - Meridional wind (m sec^{-1}) perturbations calculated using the heating function obtained by Reed and Recker (1971).

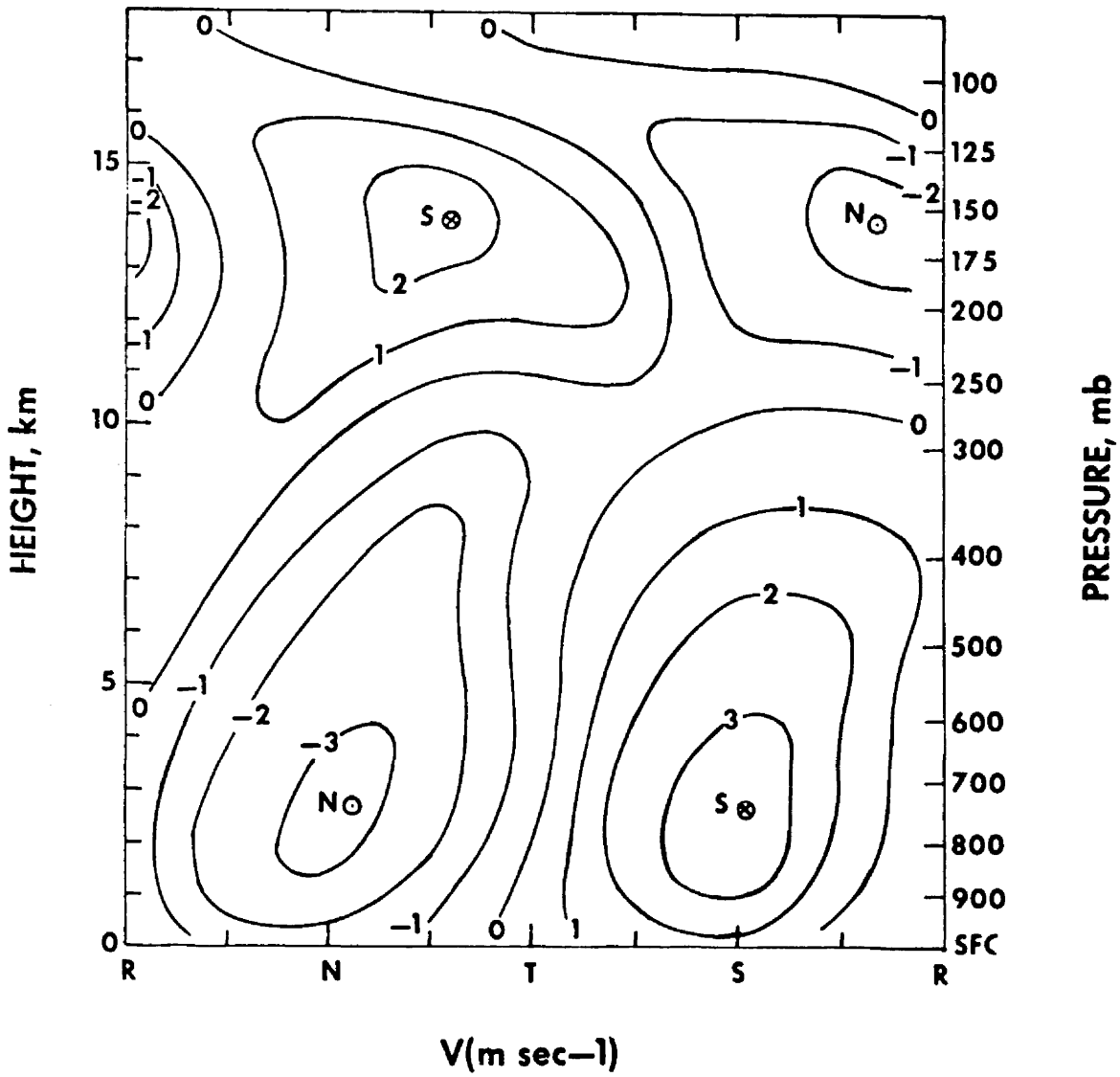

Figure 16. - Observed meridional wind (m sec^{-1}) wind field (after Reed and Recker; 1971).

Recker's compositing technique may, however, tend to average out some of the features above 500 mb since the upper level anticyclonic circulation may not always have the same phase relationship with the lower level disturbance.

The calculated and the observed temperature variations are shown in Figs. 17 and 18. The basic features are similar, although, in both cases, the temperature variations are small. The upper levels in the region of the trough appear to be slightly cooler, with a region of warmer temperatures below.

There is some discrepancy between the observed and the calculated temperature perturbations at the lowest levels. The observed structure is significantly cooler east of the trough and warmer west of it. This feature is not observed in the model, however, since with no heating or vertical motion at the boundary there will be no temperature perturbations.

The calculated and observed divergence field are shown in Figs. (19) and (20) respectively. Again, the basic structures are similar. Some care, however, must be made in interpretting these results. The heating used in the model represents a difference in the diabatic heating between the trough and the ridge. This heating was assumed to be symmetric in the longitudinal direction. Since this is probably not the case, the difference between the trough and the ridge might provide a more meaningful comparison of the divergence values. Compared in this manner, the magnitude and the vertical distribution of the observed and calculated divergence are nearly the same in the upper levels. The convergence near the lower boundary, however, is approximately 60% less than that observed.

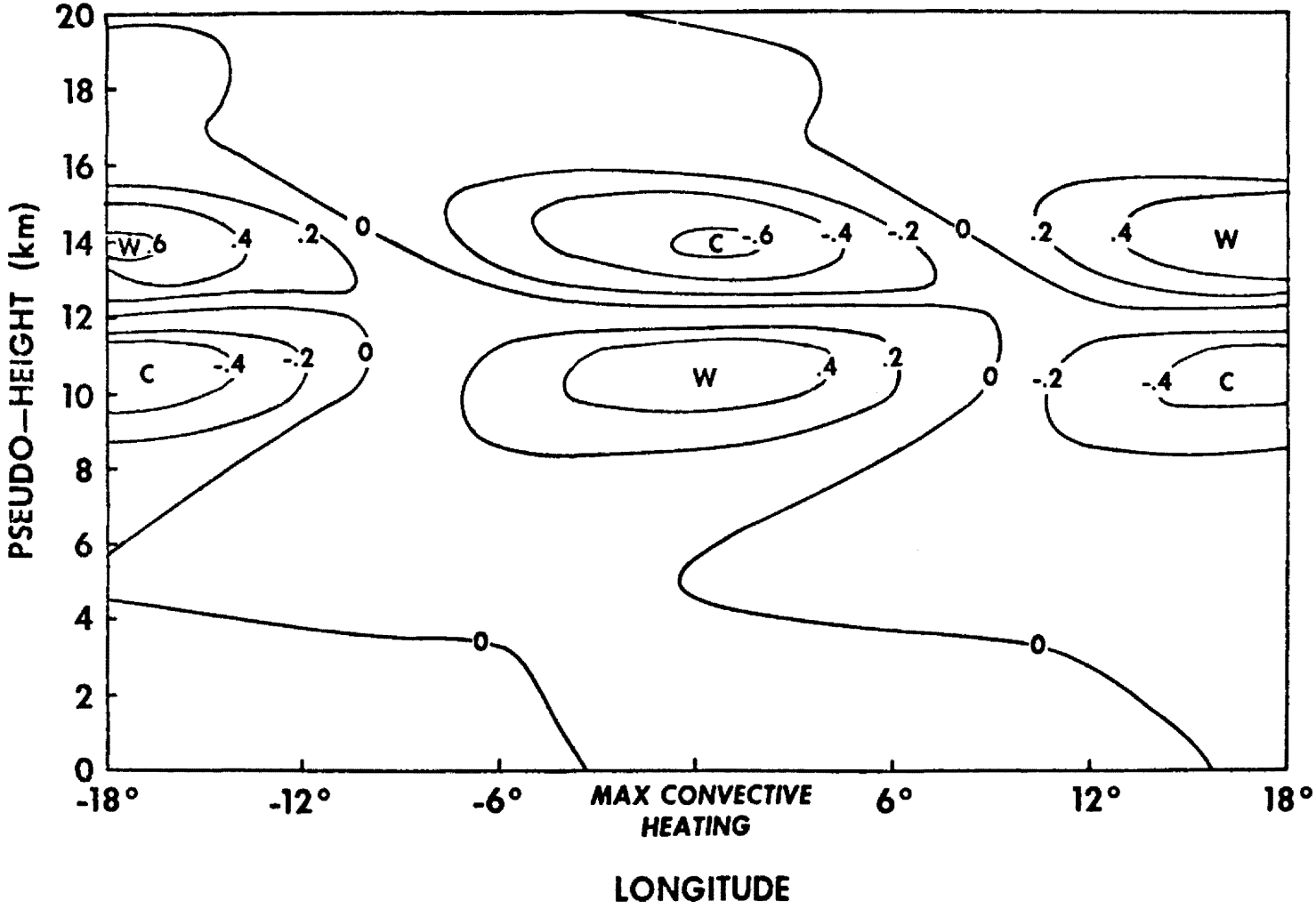

Figure 17. - Calculated temperature perturbations (^{o}C).

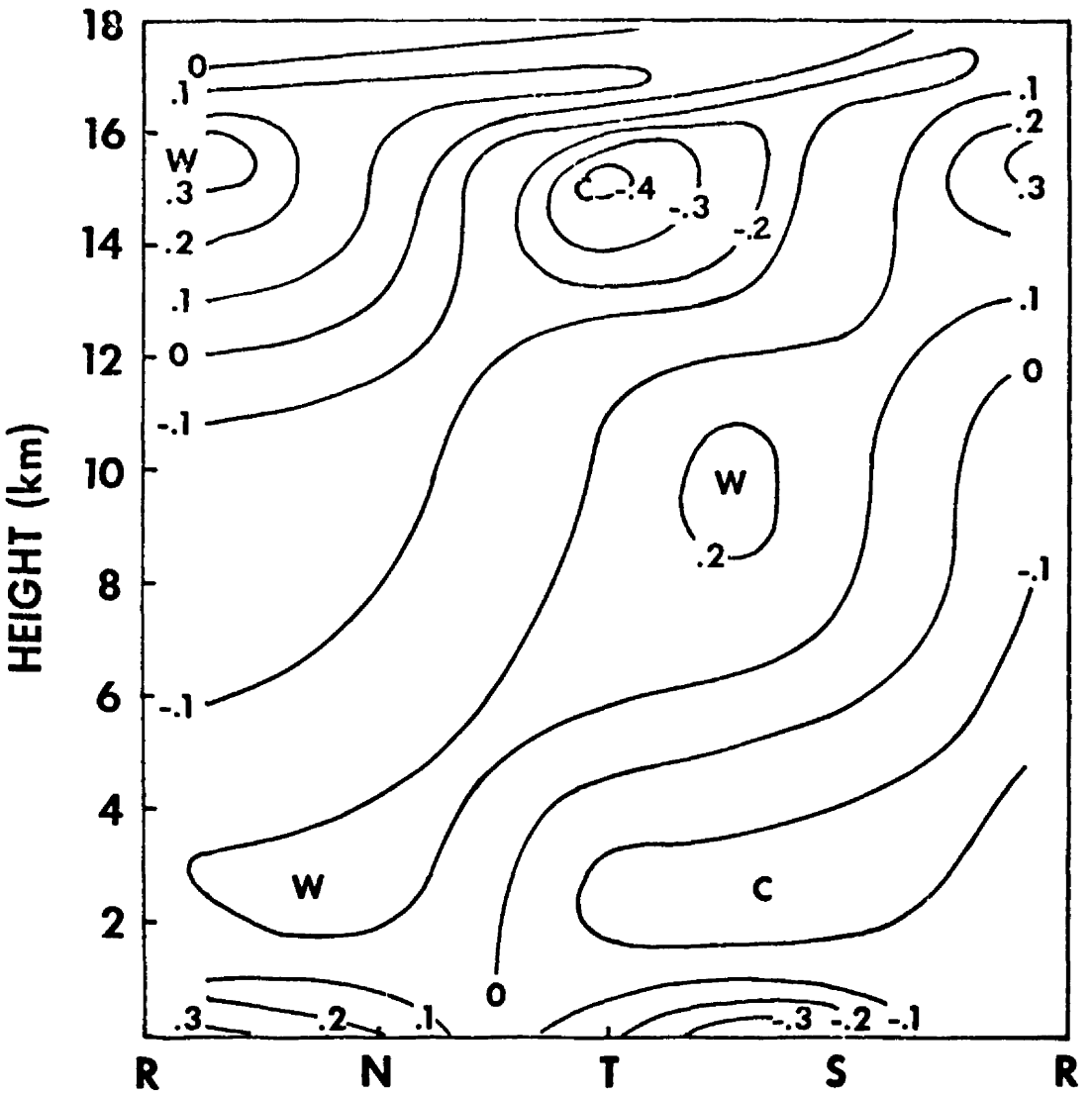

Figure 18. - Observed temperature field (^{o}C) (after Reed and Recker; 1971).

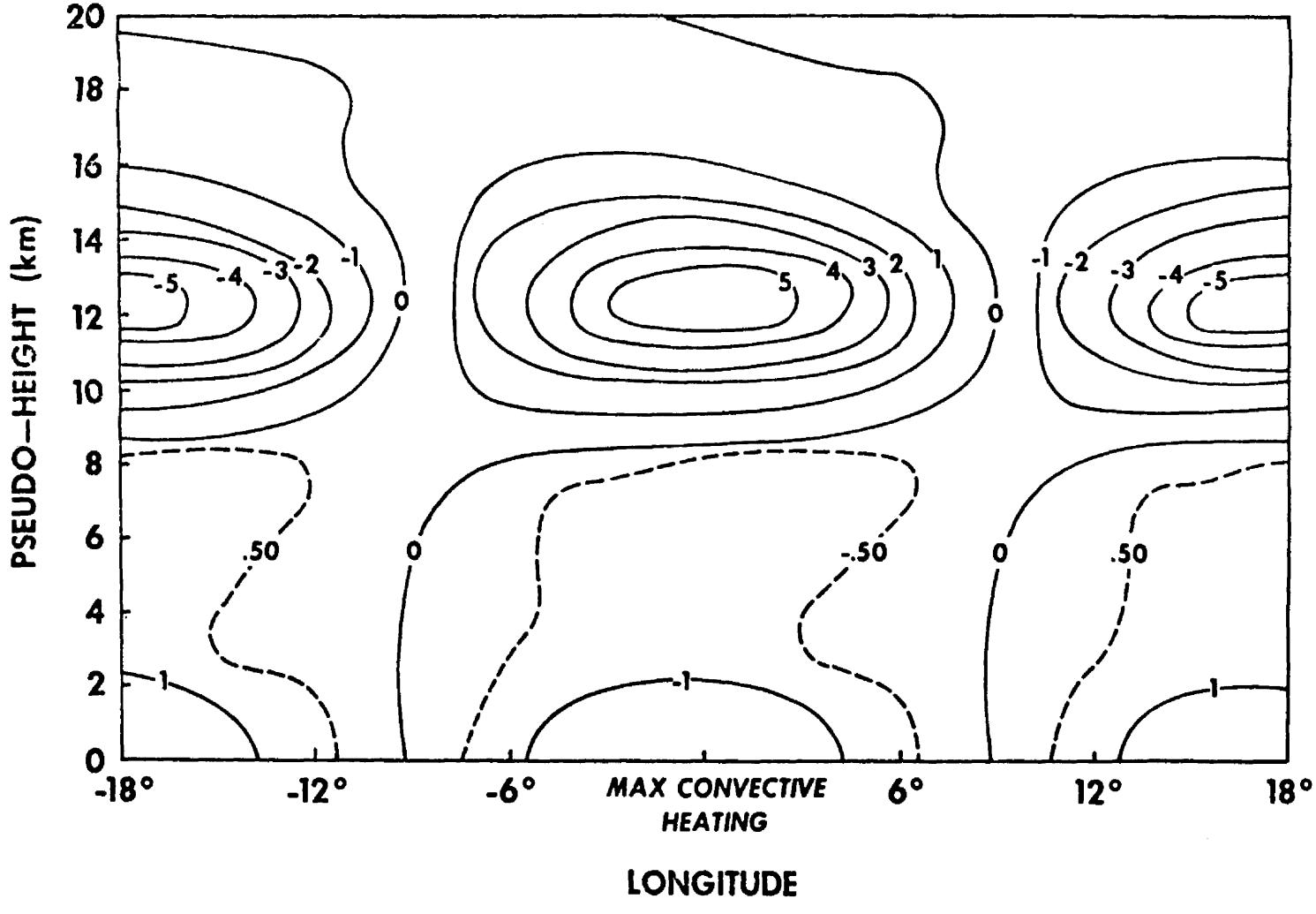

Figure 19. - Calculated divergence (x 10^{-6} sec^{-1}).

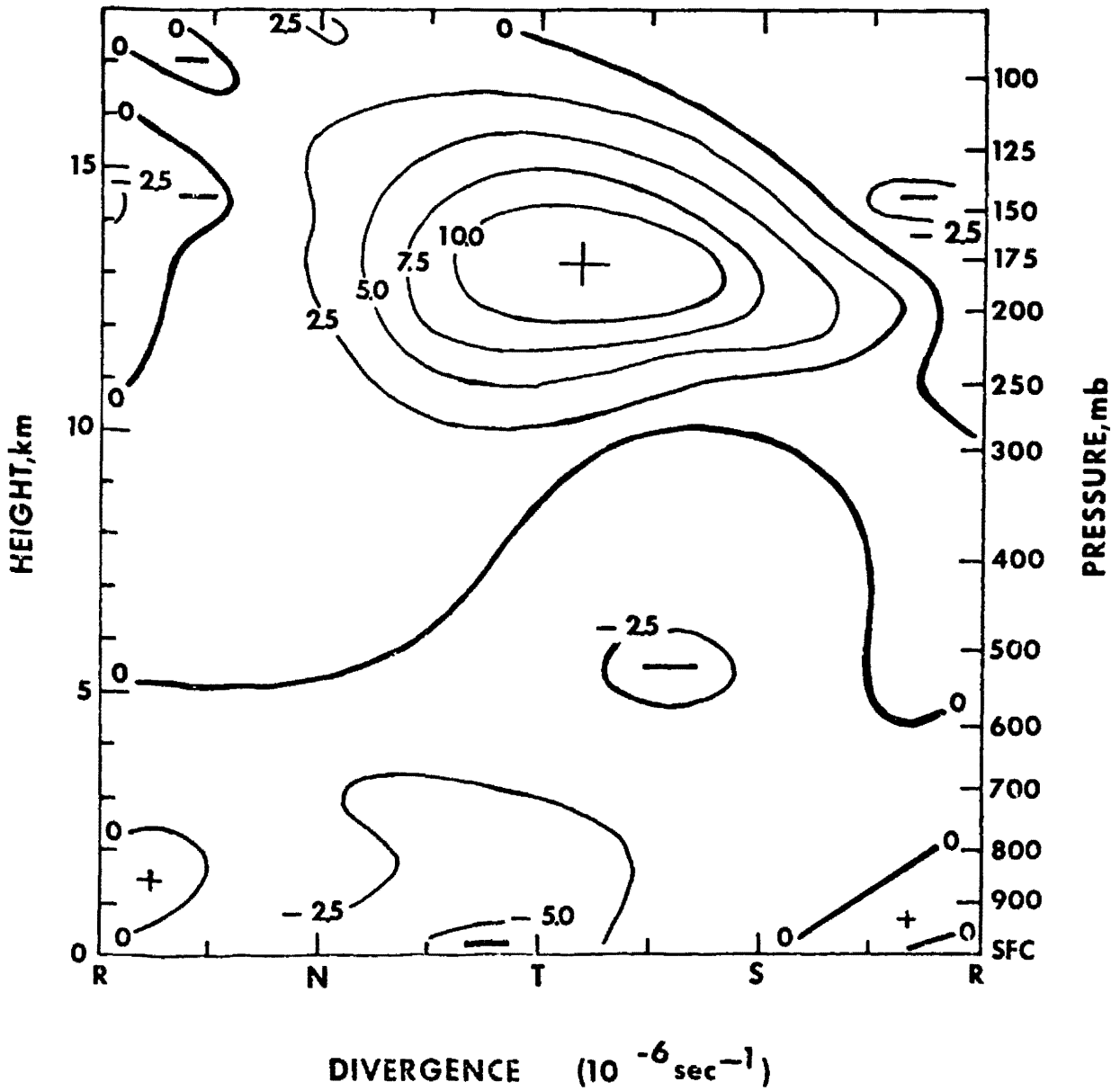

Figure 20. - Observed divergence field (after Reed and Recker; 1971).

A horizontal section of the calculated vector wind at 900 mb is shown in Fig. 21. The cyclonic nature of the flow is evident. The distribution of the north-south shear of the wind clearly indicates a cyclonic shear similar to that described by Williams (1970). There is also some indication of cross equatorial flow to the east and west of the trough. This flow pattern is in good agreement with the satellite deduced winds described by Fujita et al (1969) for the cloud clusters.

The results presented above indicate good qualitative agreement between the model results and observations. Hence, we conclude that the model may be used to investigate the response of the atmosphere to variations in the diabatic heating. The magnitude of the circulation in the lowest 8 km, however, is significantly less than that observed. The divergence profile indicates that some mechanism may be needed in the model to produce greater convergence in the lowest layers. A more exact treatment of the frictional forces at the boundary may improve the results.

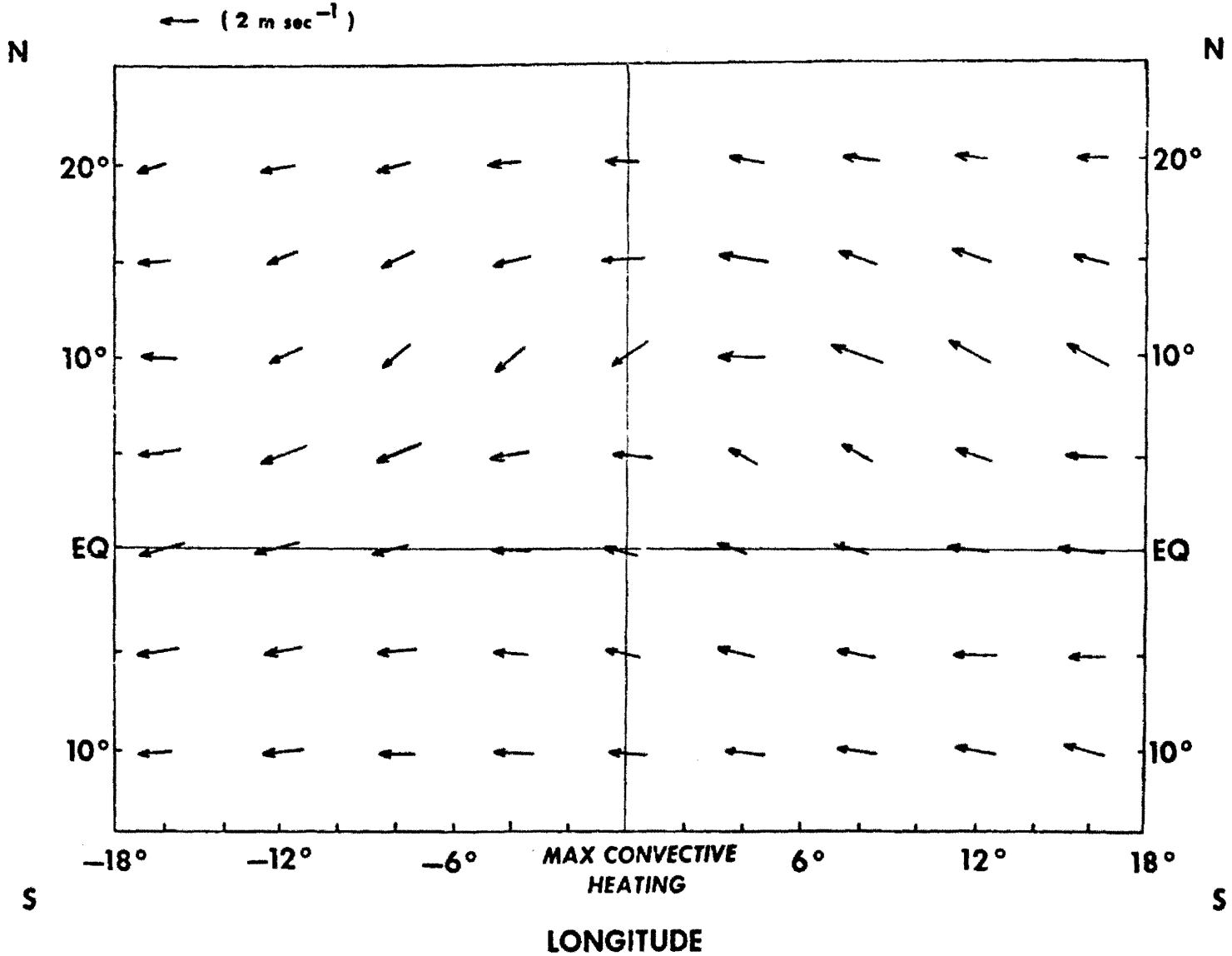

Figure 21. - Longitude-latitude section of the wind field at 900 mb.

IV. THE DYNAMIC EFFECT OF THE SPATIAL DISTRIBUTION OF CONVECTIVE AND INFRARED HEATING

The perturbed and unperturbed infrared radiation cases discussed in Chapter II suggest that variations in the type and amount of cloudiness may produce horizontal gradients of radiative heating. These gradients may be of the same magnitude as the total diabatic heating difference between the ridge and the trough of equatorial waves. If these waves are viewed as being forced by horizontal differences in diabatic heating, it is apparent that the radiation may play an important role in determining the magnitude and the structure of the wave motions.

A. Response of the Model to Infrared Heating

The model was used to diagnose the response of the atmosphere to the difference in infrared heating between the perturbed and the unperturbed infrared radiation profiles shown in Figs. 3 and 4. This difference is illustrated in Fig. 22, where the ordinate is given in units of pseudo-height ξ. The difference is nearly sinusoidal in the ξ direction, being symmetric about ξ = 8 km.

It is important to note that in using this difference in the model, the difference in heating due to shortwave radiation has been neglected. To determine the validity of neglecting the shortwave heating, the shortwave absorption by a cirrus cloud (Flemming, 1973) and the absorption by a middle level layer cloud (Korb and Moller, 1965) were determined. It was found that a maximum heating of $.7^{o}$ C day^{-1} would occur in the 150-400 mb layer. Since approximately $.1\text{-}.2^{o}$ C day^{-1} would occur in an unperturbed area, the difference is less than 15% of the infrared induced gradient and is, therefore, neglected.

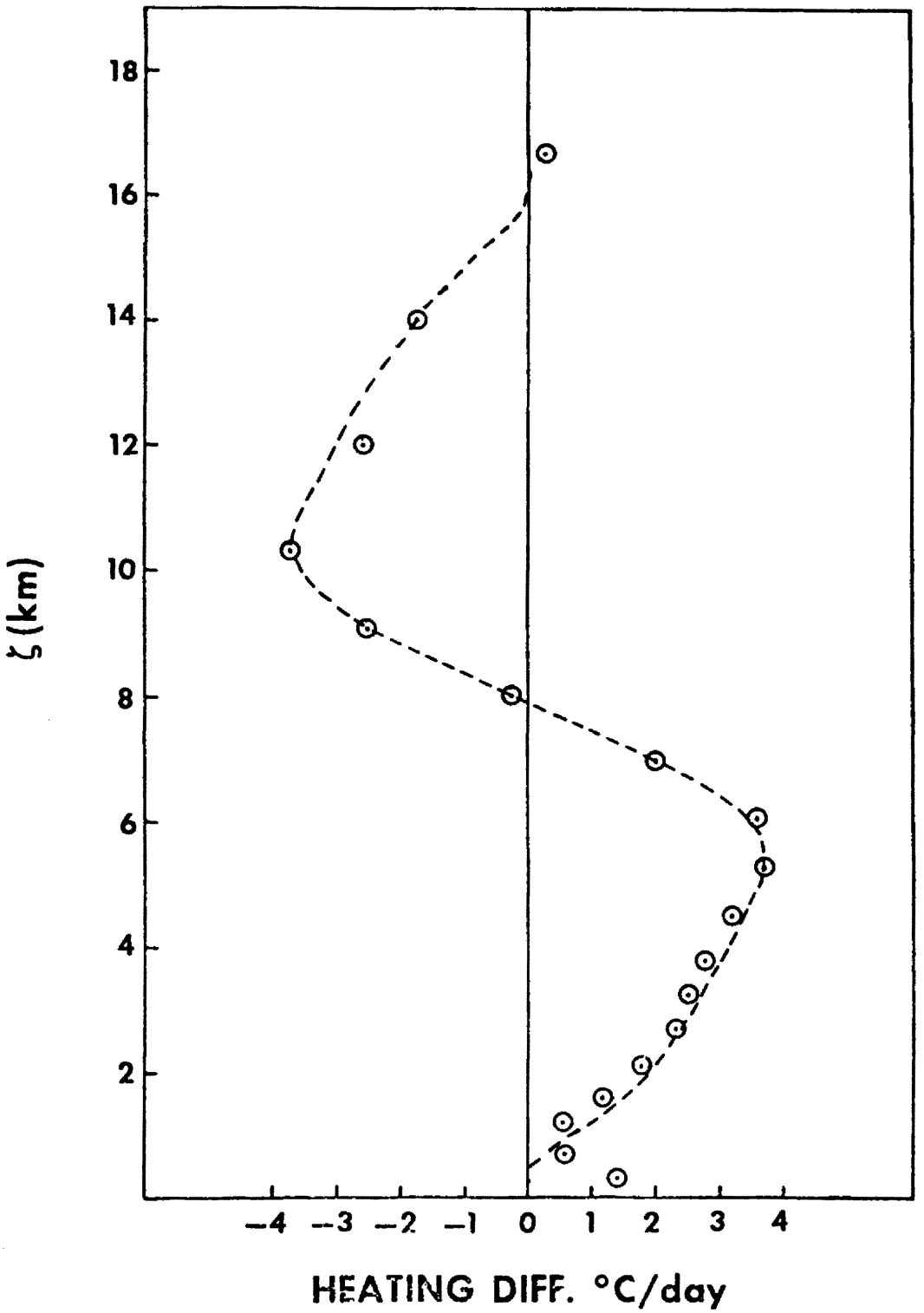

Figure 22. - Difference between observed perturbed and unperturbed heating profiles; points indicate actual differences and line represents difference used in the model.

Figure 23 is a latitude-height section of the amplitude of the meridional wind perturbations calculated using the infrared heating difference described above. Perturbations of nearly equal amplitude and latitudinal extent occur at ξ = 14 and ξ = 8 km. The maximum response occurs at a latitude of approximately 2^{o} greater than the latitude of maximum heating.

The longitude height section of the meridional wind at the latitude of maximum heating is shown in Fig. 24. From this figure, it is evident that the upper level response exhibits a cyclonic shear with respect to the perturbed infrared heating profile. The perturbation at 8 km exhibits an anticyclonic circulation. A weak cyclonic circulation is indicated near the surface.

The divergence at the region of the upper tropospheric cloud is shown in Fig. 25a. Two levels of nondivergence exist, one at 6 km and the other at 11 km. The divergence profile shown in Fig. 25a and the meridional wind structure shown in Fig. 24 suggests a circulation at the region of the upper tropospheric clouds as shown in Fig. 25b. This circulation consists of a two cell pattern, with downward motion in the upper circulation and upward motion in the middle levels. Hence, a convergence exists at the top and bottom of the troposphere, with both cells of the circulation forcing a divergence at the middle levels. In the regions away from the upper level clouds, the circulation is reversed.

As shown in Fig. 24, the meridional wind perturbations exhibit a layered structure, with alternating regions of north and south winds occurring in the troposphere. The model calculation for the radiative heating was repeated with the inclusion of a mean zonal wind similar to

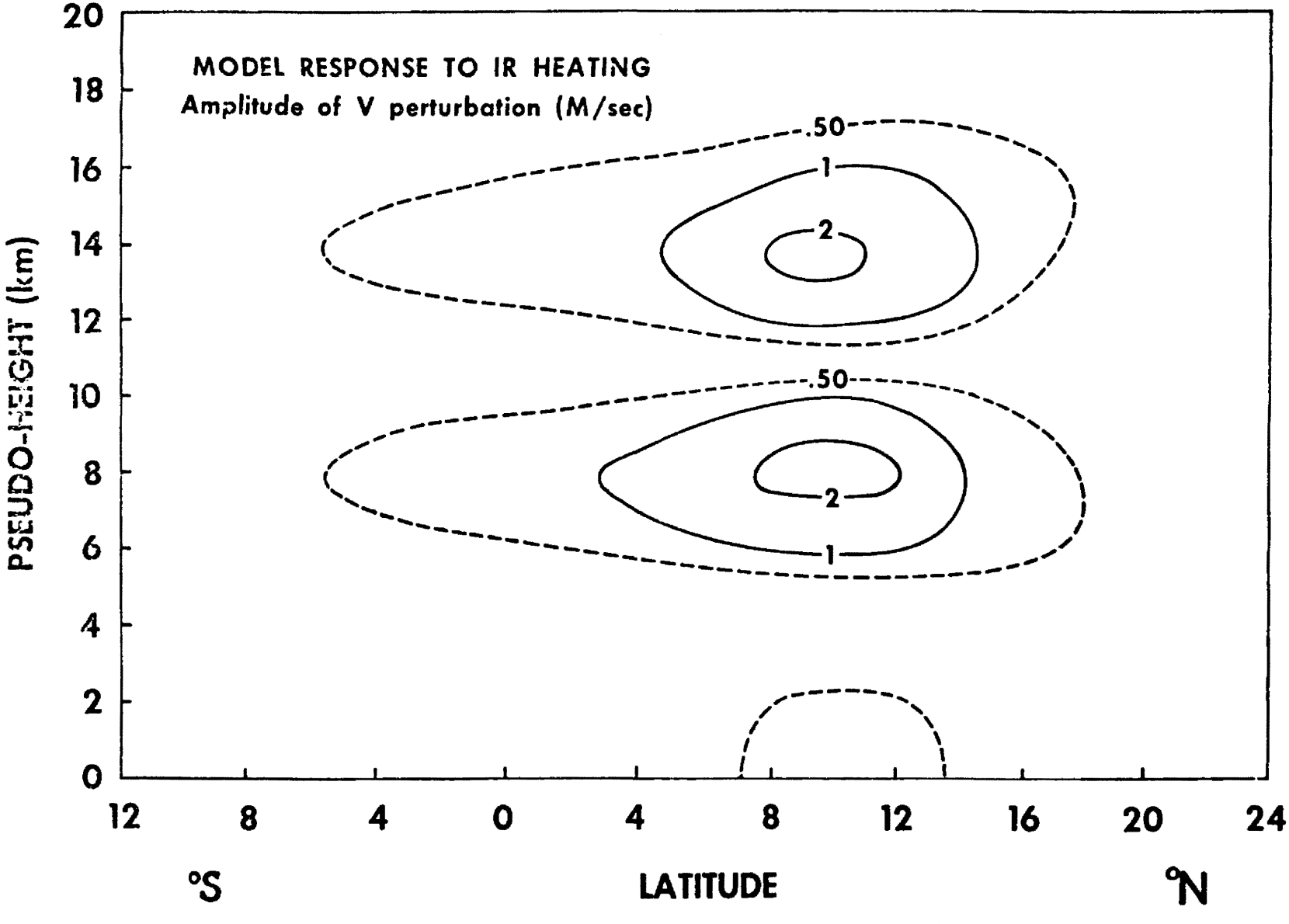

Figure 23. - Height-latitude section of the amplitude of the meridional wind (m sec^{-1}); computed using the difference shown in Figure 22.

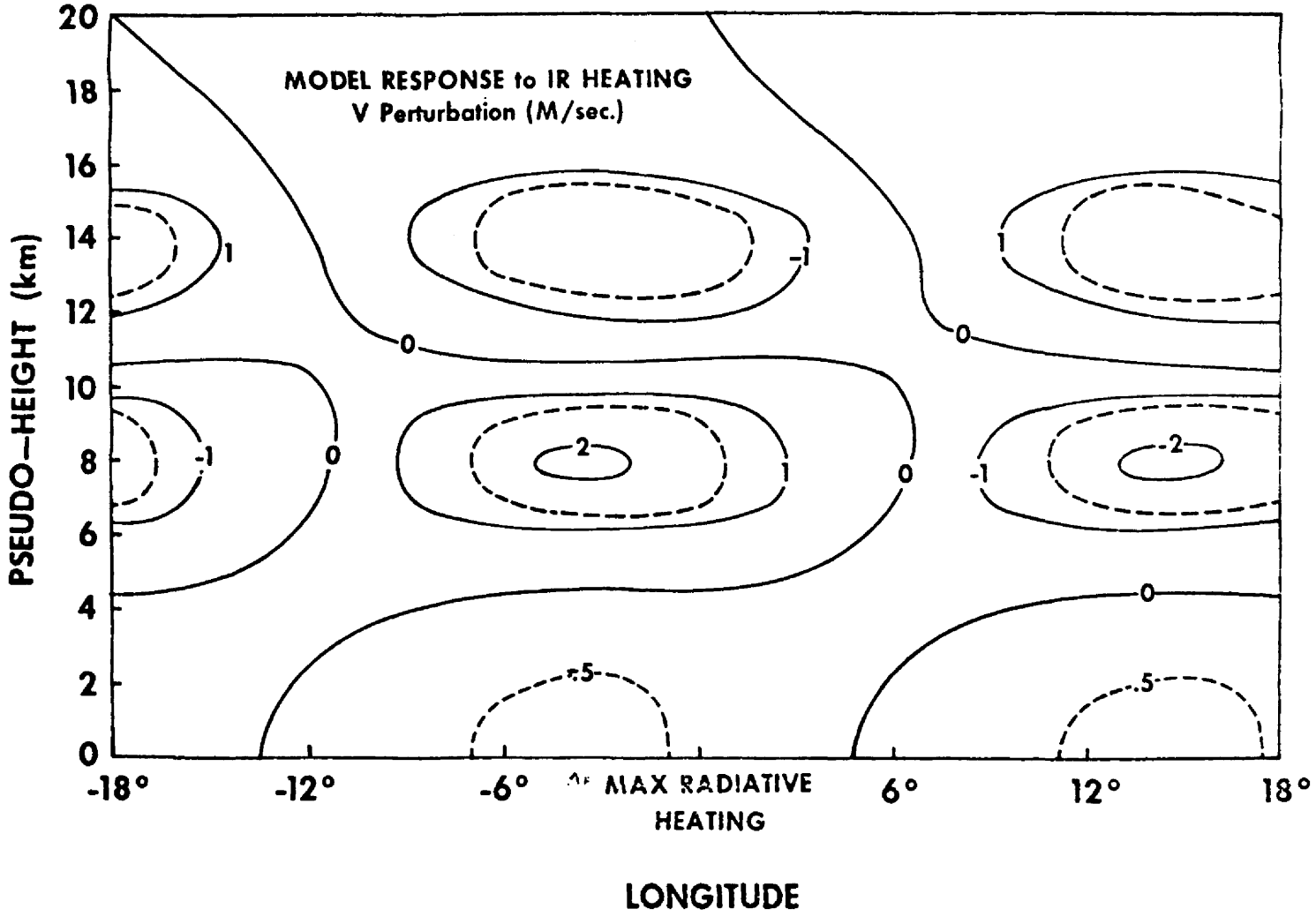

Figure 24. - Longitude-height section of the meridional wind ($m\ sec^{-1}$) with respect to the perturbed radiation case at the latitude of maximum heating.

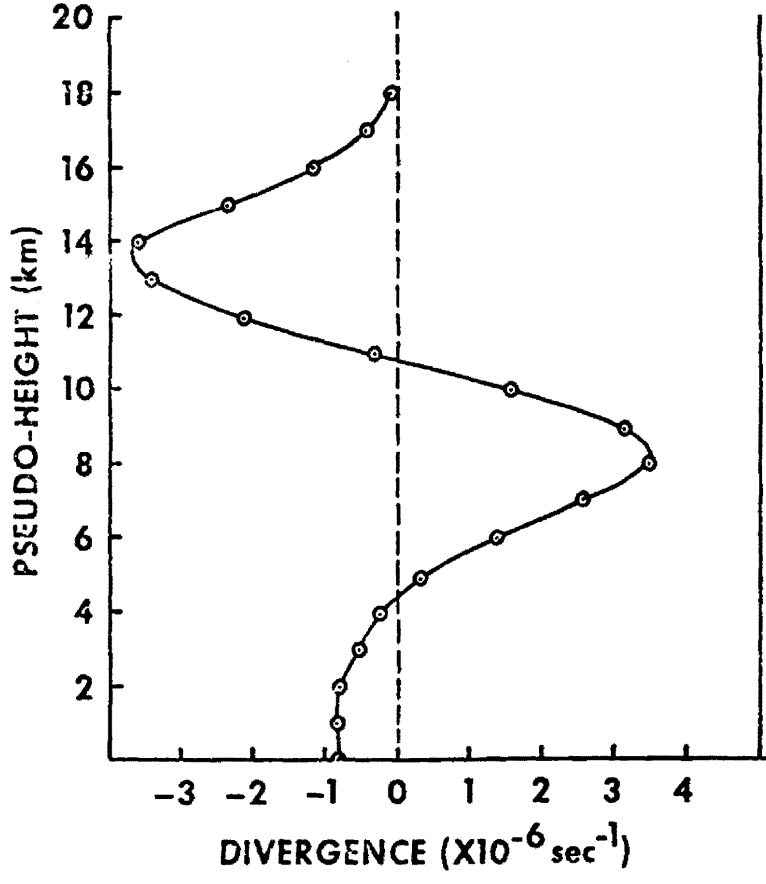

Figure 25a. - Divergence at latitude and longitude of maximum radiative heating.

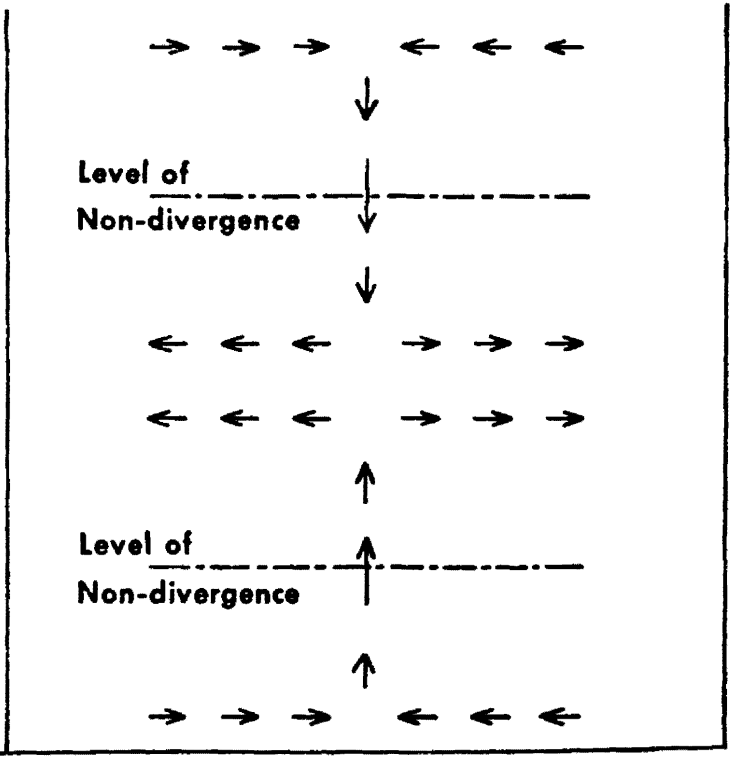

Figure 25b. - Sketch of circulation forced by the radiative heating.

that observed during the LIE. This wind field is characterized by easterlies of $\sim$10 m sec^{-1} at the surface and westerlies of $\sim$20 m sec^{-1} at 15 km and 10 m sec^{-1} at 21 km.

The meridional wind perturbations calculated at the latitude of maximum heating are shown in Fig. 26a. The magnitude of the response appears to be slightly diminished from the non-shear case. This effect, however, is primarly due to a northward displacement of the maximum upper tropospheric response. In the mid-troposphere, the vertical extent of the circulations is less than that determined for the case with no shear. Consequently, the layering of the winds becomes more pronounced in the middle troposphere.

A multi-layered meridional wind structure was observed during the LIE (Madden and Zipser, 1970) as shown in Fig. 26b. The qualitative features of the calculated structure at -12° longitude are remarkably similar to the observed structure for 00 Z, April 8. The features common to the calculations and the observations are as follows: (1) north winds at the surface, (2) south winds at 4 km, (3) north winds in the layer from 5-9 km, (4) south winds from 10 km to 16 km ($\sim$18 km pseudo-height), and (5) north winds at 17 km ($\sim$19 km pseudo-height). At all levels, however, the calculated perturbations are an order of magnitude less than the observed winds. Lindzen (1974) used wave CISK to explain the wind structure observed during the LIE.

B. Response of the Atmosphere to Variations in Infrared and Convective Heating

Tropical waves forced by horizontal differences in diabatic heating may have a structure which is sensitive to the location of the high-middle

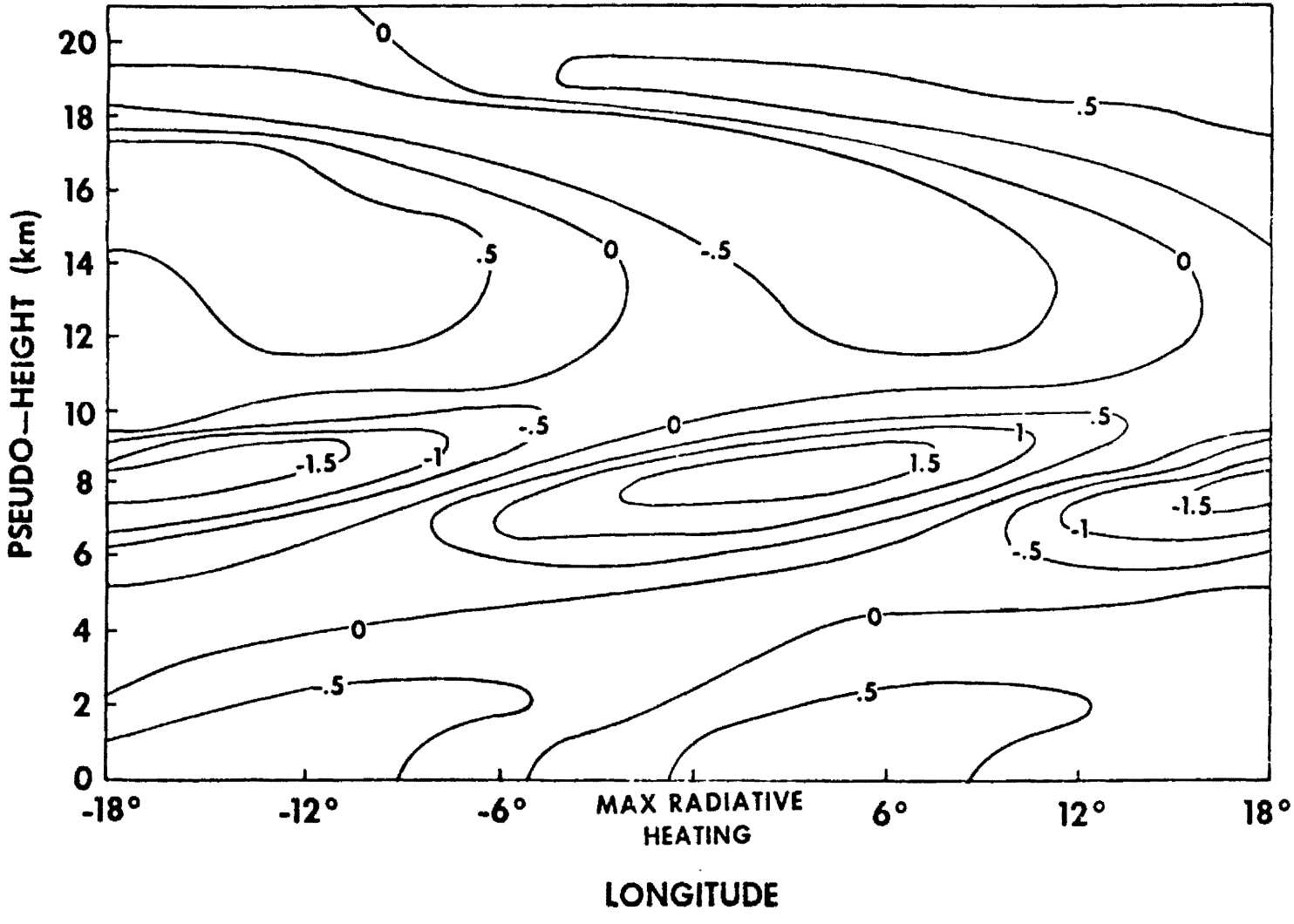

Figure 26a. - Same as Figure 23, but with shear.

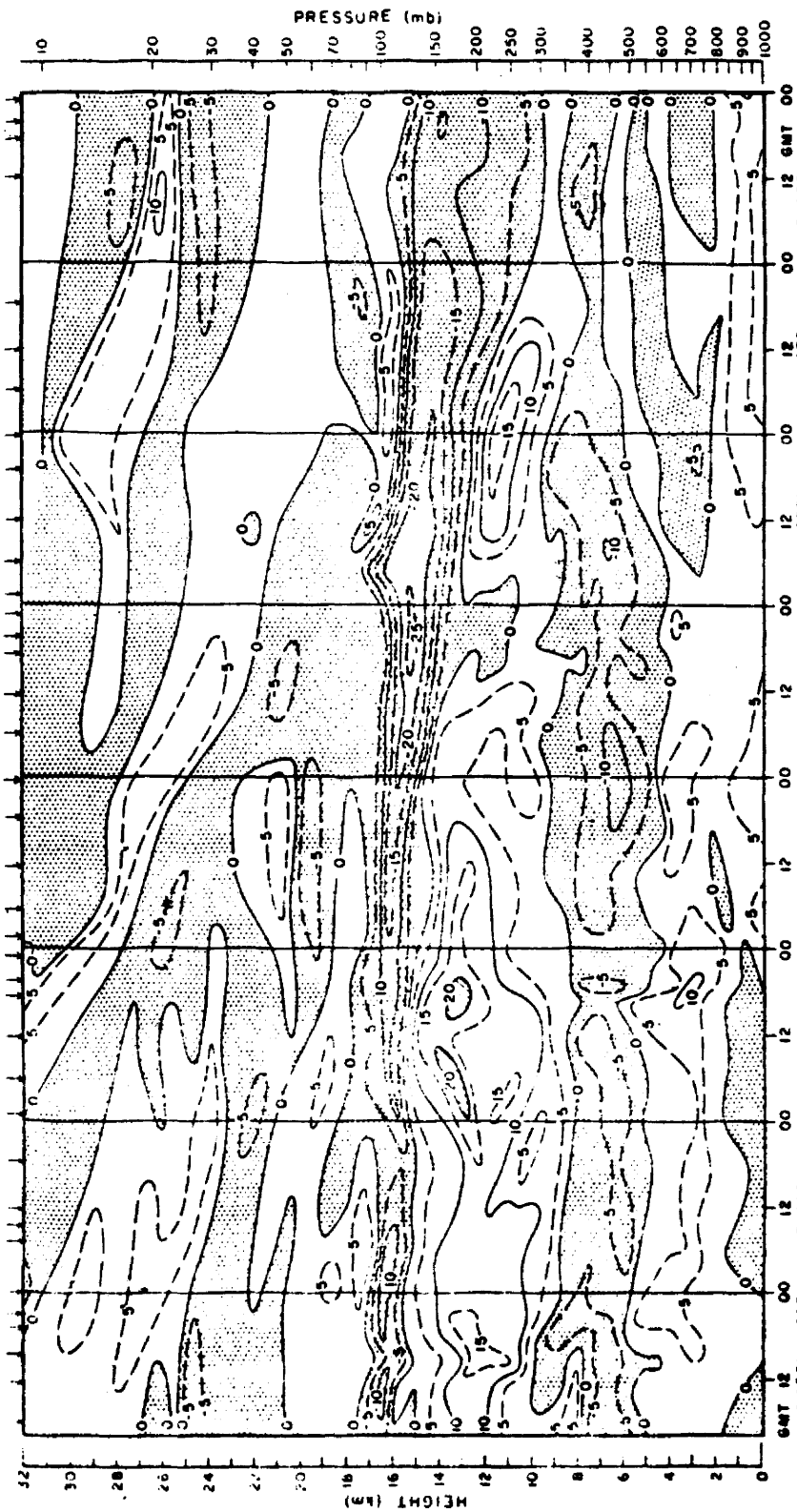

Figure 26b. - Vertical time section of the V component of the wind (m sec^{-1}) at Palmyra. (after Madden and Zipser, 1970).

cloud with respect to the convective heating. The persistence in time of layered clouds, particularly cirrus decks, allows the upper tropospheric clouds to exist in regions where there may be very little convective activity. During the LIE, for example, there was some indication that the perturbed radiative cases occured 24-36 hours after rainfall was recorded at Palmyra.

There are at least two possible means by which spatial differences in the convective and radiative heating may be maintained. For example, intense convection may be a source region for the upper level clouds. Thus, spatial differences in the heating components will be determined by the life-time of the upper level clouds, the motion of the convection, the wind shear and the temperature and moisture field. Similarly, the upper tropospheric clouds may be associated with an upper tropospheric wave. The meridional wind at 250 mb and 350 mb observed from March 22 to April 16 at Palmyra during the LIE is shown in Fig. 27. During the first two weeks of this period, the perturbed radiative heating has a constant phase relationship to a wave in the meridional wind field. As shown by the spectral wave studies (Wallace, 1971), the upper tropospheric waves may have varying phase relationships to the disturbances in the lower troposphere; these differences in the phase of the wave would provide a mechanism for varying the phase relationship between the radiative and convective heating.

The large-scale model described previously was used to diagnostically determine the effect that various diabatic heating profiles might have in determining the structure of the tropical wave motions. The heating profiles were determined by combining the convective and radiative heating with varying phase differences.

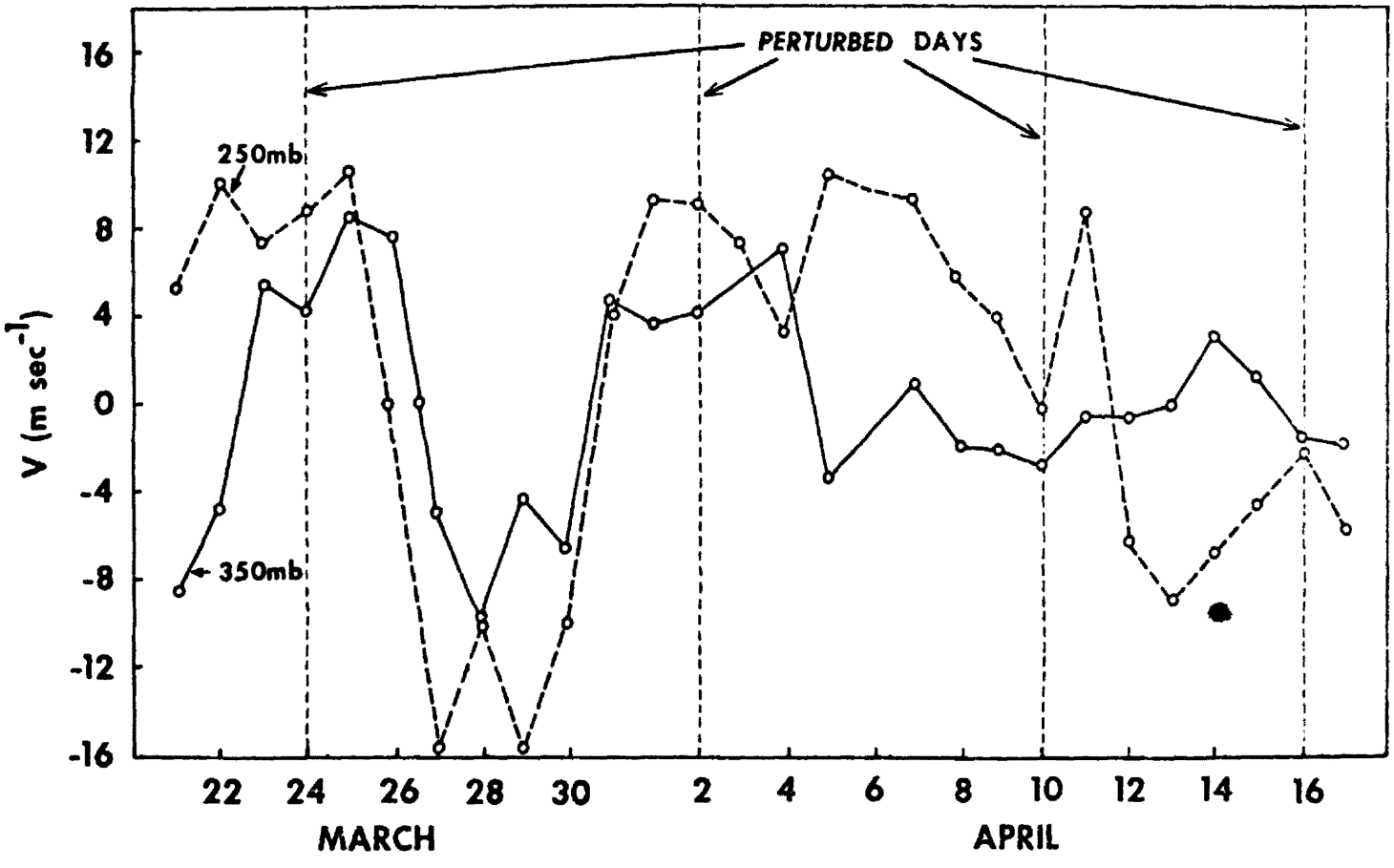

Figure 27. - Meridional wind at 250 mb and 350 mb, observed during LIE, 1967.

The radiative and convective heating used in the model are shown in Figs. 7 and 22. These heating profiles were considered to represent a maximum horizontal difference. Consequently, one half of the heating functions were used as the amplitude.

Several model computations were made with the convective and radiative heating having different phase relationships. For the cases considered, the radiative heating has phases relative to the convective heating of 0, $\frac{\pi}{4}$ $\pi/2$, $3\pi/4$ and π (positive phase indicates that the radiative heating is located west of the convective heating). The amplitude and phase of the meridional wind perturbations as determined from these calculations is shown in Figs. 28a and 28b. These perturbation quantities were determined at a latitude of 8.6° N, the latitude of maximum heating. The largest variations occur at 14 km. With the high-middle cloud centered over the convective heating, the meridional wind at 14 km has an amplitude of 1 m sec^{-1}. With the high-middle cloud centered a half wavelength out of phase with the convective heating, the amplitude is 5.5 m sec^{-1}. Similar changes occur at the lower levels, although the changes are only half as great.

The phase of the meridional wind perturbations (Fig. 28b) is nearly constant with height for all cases. With the exception of the circulation at 4-8 km, there is also little variation in the phase for the different heating patterns. In the middle troposphere, however, the phase differences between the perturbations are approximately equal to the phase differences between the convective and radiative heating.

The calculated divergence is shown in Fig. 29. This calculation was made at the latitude and the longitude of the maximum convective heating.

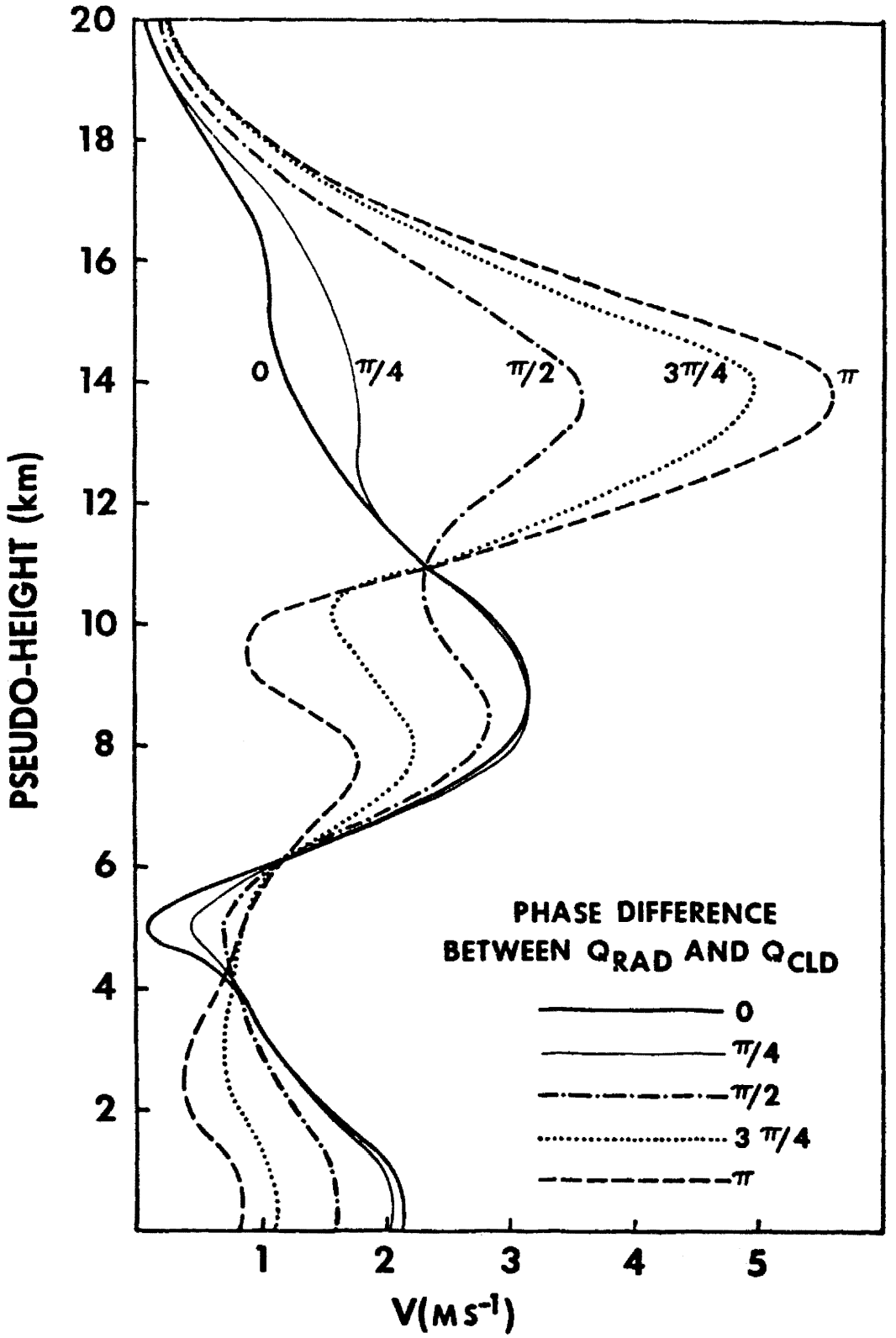

Figure 28a. - Amplitude of the meridional wind perturbations at the latitude of maximum convective heating. The phase is the phase difference between the perturbed infrared heating and the convective heating.

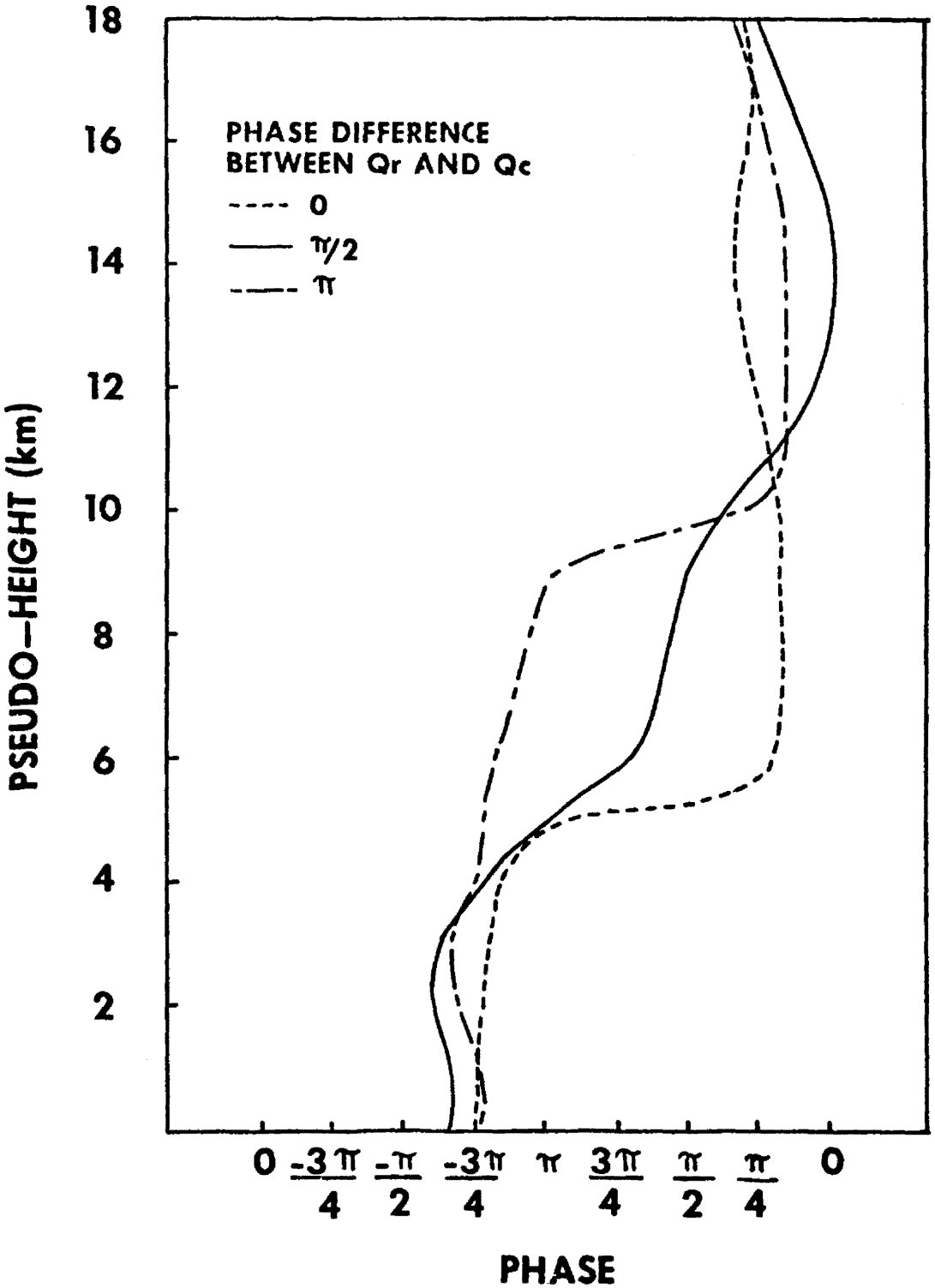

Figure 28b. - Phase of the meridional wind perturbations.

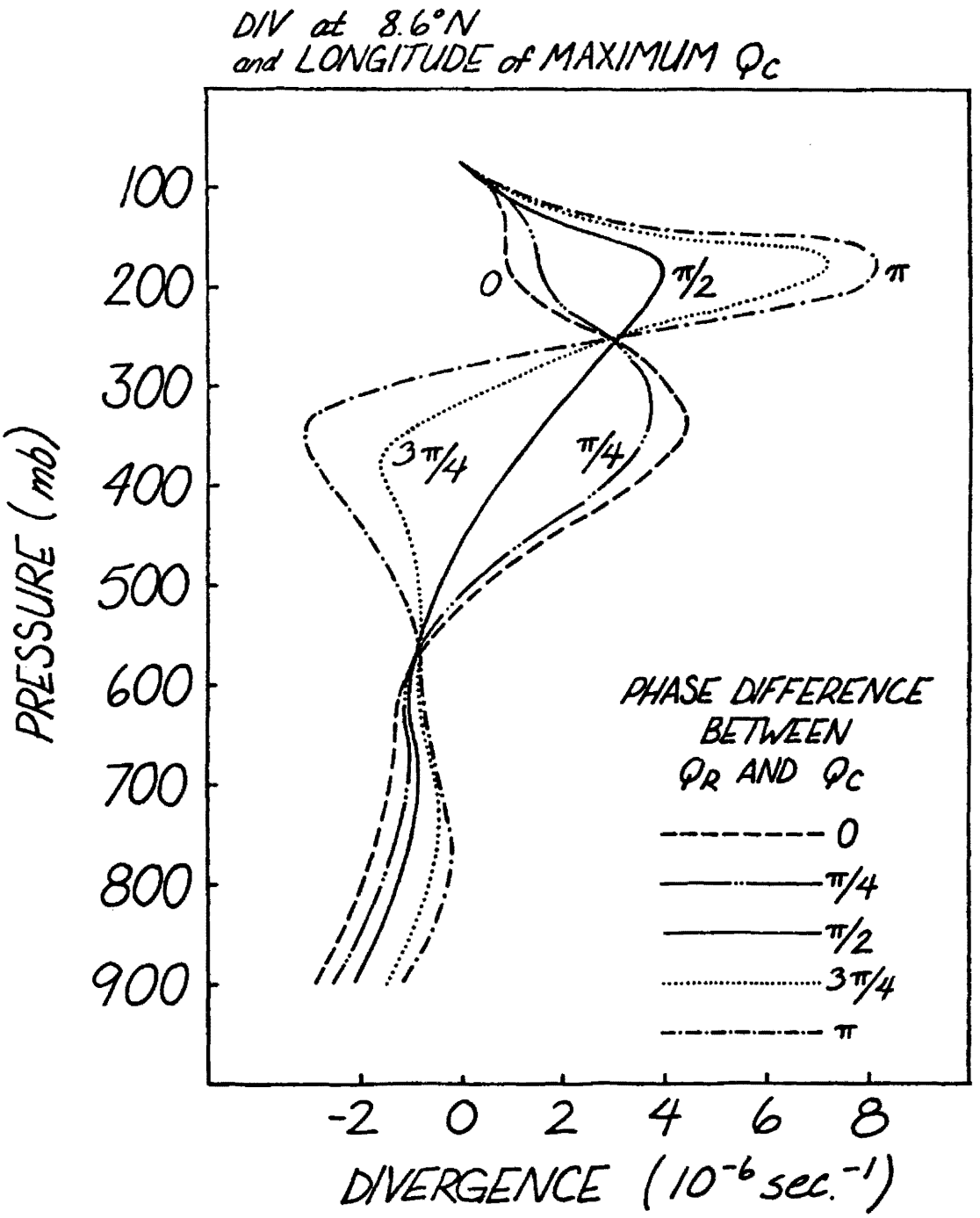

Figure 29. - Divergence for various phases of convective and radiative heating functions. Divergence calculations are made at latitude and longitude of maximum convective heating.

For all cases, there is convergence in the lowest 350 mb. The convergence at 900 mb varies from -3×10^{-6} sec^{-1} for the 0 phase difference to -1.5×10^{-6} sec^{-1} for the π phase difference.

With the high-middle cloud located over the convective heating, there is divergence from 550 mb to the tropopause. The maximum divergence occurs at approximately 350 mb, and has a magnitude of 4×10^{-6} sec^{-1}. For the π phase difference case, the maximum occurs at 200 mb, with a magnitude of 8×10^{-6} sec^{-1}.

From Fig. 29, it is apparent that the most significant effect of varying the phase of the radiative and convective heating is to vary the height of the upper level divergence maximum and the level of nondivergence. For the case when the upper level clouds are centered over the convective heating, the level of nondivergence occurs near 500 mb. Hence, for this case, the maximum vertical velocities would also occur at this level. When the radiative cloud is centered a half of a wavelength from the convective heating, the level of maximum vertical velocity at the region of the convection occurs near 300 mb.

The calculations made above for various phases of convective and radiative heating were made with no vertical shear of the mean zonal wind. Holton (1971), however, has shown the structure of waves forced by the diabatic heating to be sensitive to the shear. To determine how the vertical shear might interact with differences in the radiative and convective heating, a mean zonal wind profile was specified and model calculations for the different heating functions were repeated. As for the case with no shear, the clouds associated with the radiative heating are assumed to have a spatial location which is independent of the wind field.

The wind profile used in the model is the wind profile determined by Reed and Recker (1971) for the KEP triangle (Fig. 14). This wind profile is characterized by easterlies increasing from $\sim$ 2 m sec^{-1} at the surface to 9 m sec^{-1} at the tropopause.

The amplitude and phase of the meridional wind perturbations calculated with shear are shown in Fig. 30a and Fig. 30b. The amplitude of the perturbations differ by less than 15% from the non-shear cases. The phase, however, differs significantly from the previous computations. For the non-shear cases the phase was nearly constant with height. With shear included, the phase tilts westward with height in the lowest 3 km and eastward with height from 3 km to 13 km; above 13 km, there is westward tilt with height. The effect of the shear on the longitudinal structure (i.e. the phase), however, is approximately independent of the heating function considered.

The divergence at the latitude and longitude of the maximum convective heating is shown in Fig.31 for the case with shear. These profiles vary by less than 15% from the non-shear cases shown in Fig. 29.

Calculations were made with a vertical shear which was twice as great as that used in the model calculations above. For these cases, the divergence profile changed only slightly (<15%) from the weak shear and non-shear case. Significant changes, however, occured in the structure of the wind fields. These changes, however,do not show a strong dependence on the heating distribution and are in agreement with the results shown by Holton (1971) for the case with easterly shear.

Wind profiles with vertical shears greater than twice the shear for the KEP were tested in the model. When the large shears are used in the model, however, noticable distortion of the wind fields occurs at the

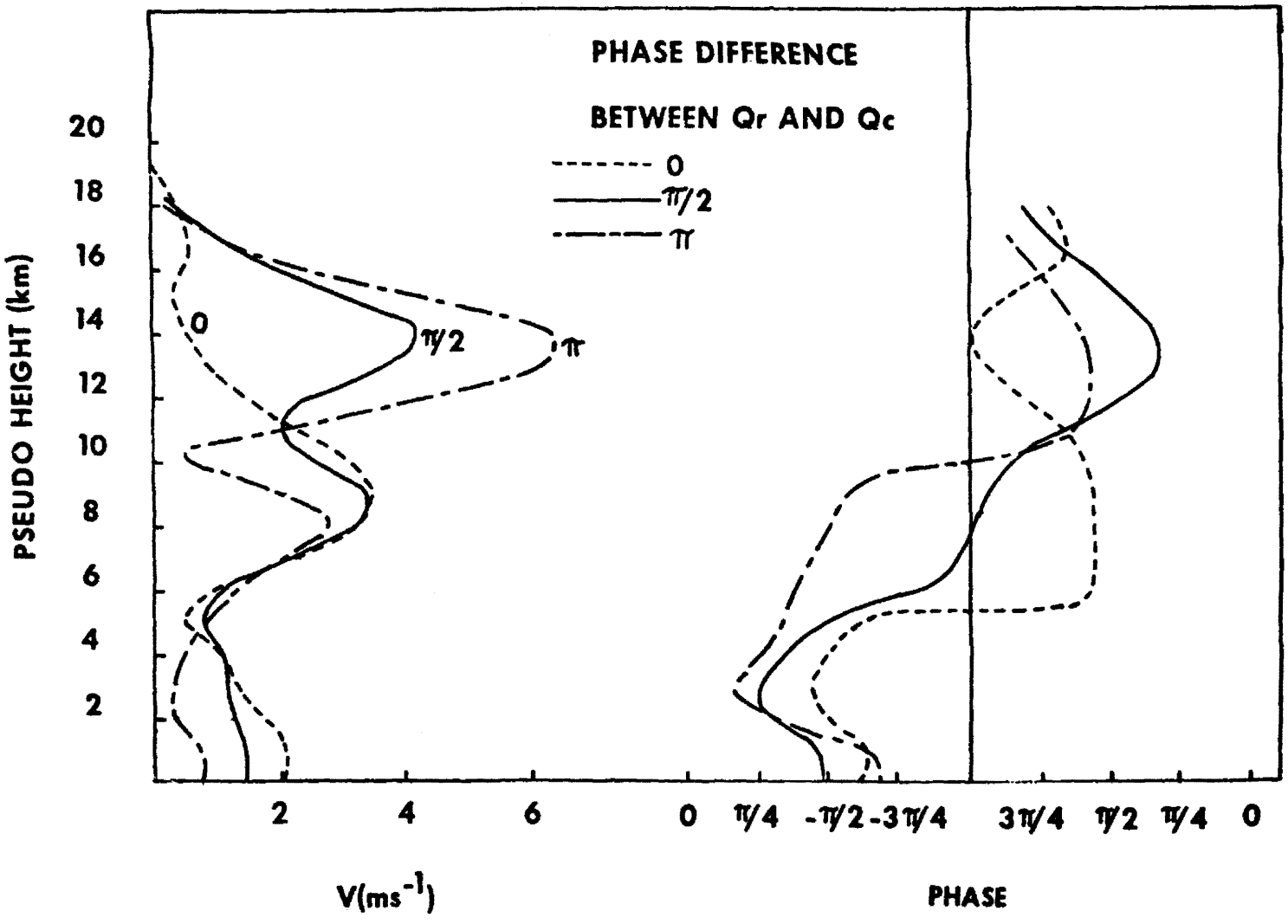

Figure 30a. - Same as Figure 28a but with shear.

Figure 30b. - Same as Figure 28b but with shear.

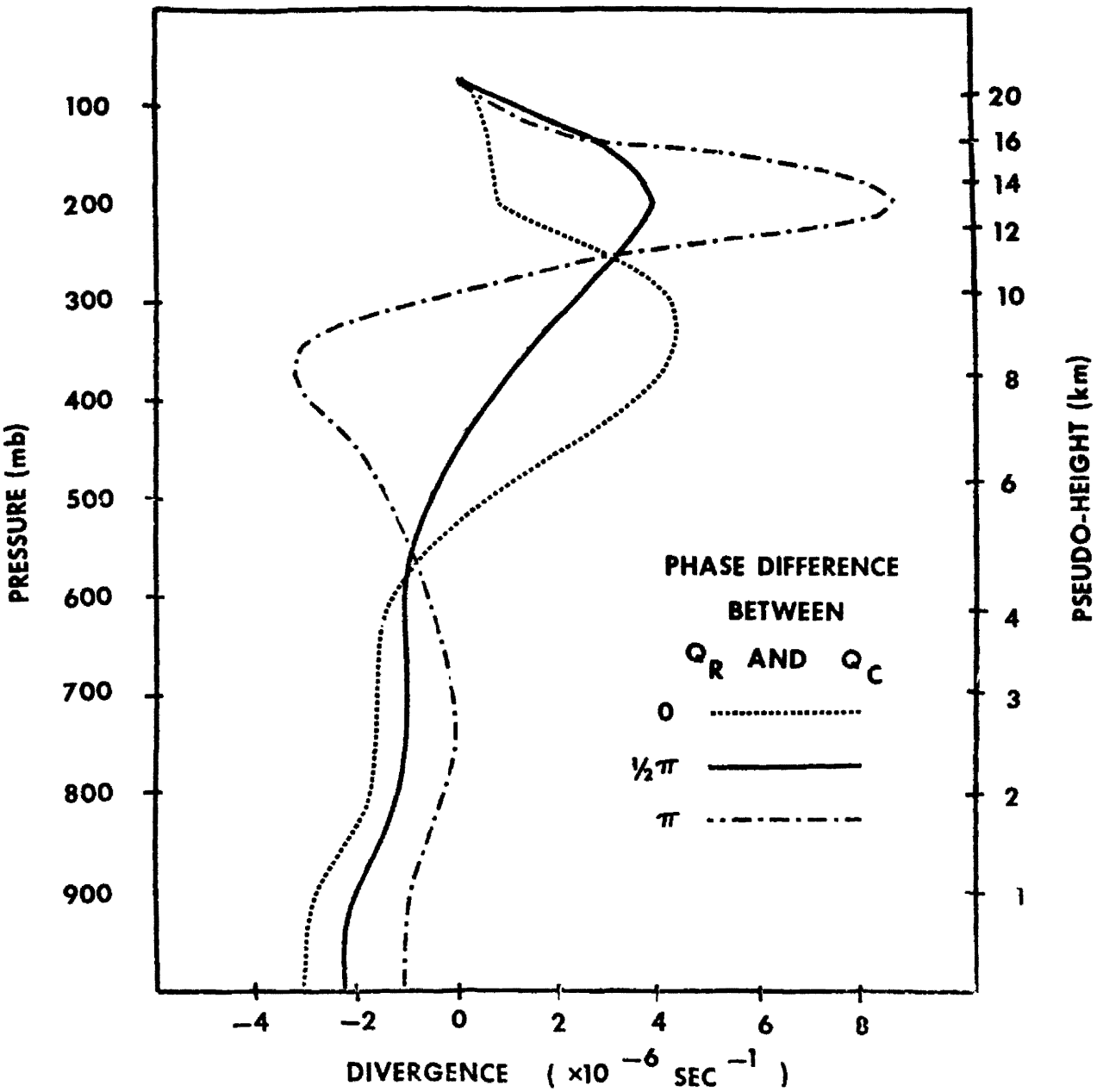

Figure 31. - Same as Figure 29 but with shear.

upper boundary. Furthermore, if the vertical motion is large, the term $w \frac{\partial \overline{u}}{\partial \xi}$, which was ignored in the formulation of the model, may become significant compared to the other terms in the momentum equation. Hence, the results calculated using large shear may not be consistent with the approximation of dropping the term $w \frac{\partial \overline{u}}{\partial \xi}$

V. CONCLUSIONS

A large-scale model is used to determine the effect of various diabatic forcing functions on low latitude tropospheric motions. The model consists of the horizontal momentum equations, hydrostatic equation, continuity equation and thermodynamic equation combined into a single partial differential equation. The diabatic heating is specified and the differential equation is solved numerically to determine the response of the atmosphere to the forcing. Many of the features of tropospheric equatorial waves are duplicated by using the observed differences in the heating between the trough and ridge of the waves in the model.

During the Line Island Experiment, 1967, infrared heating rates determined from radiometersonde measurements exhibit temporal differences of $4\,^{\circ}C\ day^{-1}$ at individual levels in the atmosphere. These differences result from high-middle cloudiness occuring every six to eight days.

The structure of waves forced by the observed differences in radiative heating was determined. The results show that radiative heating and strong westerly shear cause the meridional wind field to respond in a manner which is in good qualitative agreement with the meridional wind field observed during the LIE. The magnitude of the perturbations, however, are significantly less than the observed winds. When the radiative heating was combined with convective heating the vertical structure of the forced motions were found to be very sensitive to the phase difference between the convective and the radiative

heating. The amplitude of the meridional wind perturbations at 200 mb ranged from 1 m sec^{-1} for the case when the radiatively active upper tropospheric clouds were centered over the convective heating to 5.5 m sec^{-1} when the upper tropospheric cloud was centered a half of a wavelength from the convective heating. For the same cloud configurations, the divergence at 200 mb varied from 1×10^{-6} to $8 \times 10^{-6} sec^{-1}$ at the region of the maximum convective heating.

Varying the vertical shear from zero to twice that reported by Reed and Recker (1971) did not significantly alter the model's response to the phase difference between the radiative and convective heating functions.

The diagnostic wave model is shown to be a useful tool for investigating the sensitivity of the atmosphere to a specified heating and zonal wind. A prognostic approach to the problem, however, would allow the heating to be a function of the large-scale motion fields. Such a treatment would be needed to theoretically study the effect of the cloud modulated infrared heating on the growth and decay of the tropical wave systems.

The results of this study indicate that the radiative heating is a significant component of the diabatic heating. More investigation, however, is needed to determine the exact role of radiation in it relationship to the dynamic features of the tropics. For example, additional observations of the radiative effect of the upper level clouds would allow a more accurate description of the radiative heating fields important to the large-scale dynamics. If these

measurements are made in conjunction with measurements of the large-scale wind, temperature, and moisture fields, information may be obtained as to how the growth and structure of the tropical clouds systems vary with different configurations of convective and radiative heating. The results of such a study might easily be expressed in terms of a forecast technique, particularly since the location and movement of the upper troposphere clouds are easily monitored from satellites.

REFERENCES

Arakawa, A. and W. Schubert, 1974: Interaction of a cumulus cloud ensemble with the large-scale environment. Part I. to be published in J. Atmos. Sci.

Chang, C. P., 1970: Westward propogating cloud patterns in the tropical Pacific as seen from time-composite satellite photographs. J. Atmos. Sci., 27, pp. 133-138.

Cox, S. K., 1969a: Infrared radiation models for the tropics. Radiation in the Free Atmosphere, University of Wisconsin, pp. 8-26.

Cox, S. K., 1969b: Observation of infrared effective emissivities of cloud layers. Radiation in the Free Atmosphere, Univ. of Wisconsin, pp. 27-37.

Cox, S. K., 1973: Infrared heating calculations with a water vapor pressure broadened continuum; Quart. J. Roy. Meteor. Soc., 99, pp. 669-679.

Fleming, J. R., 1973: Radiative effects of cirrus clouds. Atmospheric Science Paper No. 207, Dept. of Atmospheric Science, Colorado State University, Fort Collins, Colorado, 64 pages.

Forsythe, G. and B. Moler, 1967: Computer solutions of linear algebraic systems. Englewood Cliffs, New Jersey, Prentice Hall Inc., 141 pages.

Fujita, T., K. Watanabe, and T. Izawa, 1969: Formation and structure of equatorial anticyclones caused by large-scale cross equatorial flows determined by ATS-I photographs. J. Appl. Meteor., 8, pp. 649-667.

Gray, W. M., 1972: Cumulus convection and larger-scale circulations. Part II, Paper Number 190, Department of Atmospheric Science, Fort Collins, Colorado, 80 pages.

Hayashi, Y., 1970: A theory of large-scale equatorial waves generated by condensation heating and accelerating zonal wind. J. Meteor. Soc. of Japan, 48, pp. 140-160.

Holton, J. R., 1971: A diagnostic model for equatorial disturbances. The Role of Vertical Shear of the Mean Zonal Wind. J. Atmos. Sci., 28, pp. 55-64.

Holton, J. R., 1972: An Introduction to Dyanmic Meteorology. Academic Press, New York, 319 pages.

Korb, G. and F. Möller, 1962: Theoretical investigation of energy gain by clouds. Final Technical Report, Ludwig-Maximilians Universitat, Meteorologisches Institut Munchen, Germany, 185 pages.

REFERENCES - Continued

Lindzen, R. S., 1974: Wave CISK in the tropics. J. Atmos. Sci., 31, pp. 156-179.

Lindzen, R. A. and H. L. Kuo, 1969: A reliable method for the numerical solution of a large class of ordinary and partial differential equations. Mon. Wea. Rev., 97, pp. 732-734.

Liou, Kuo-Nan, 1973: A numerical experiment on Chanclasekhar's Discrete-Ordinate method for radiative transfer. Applications to cloudy and hazy atmospheres. J. Atmos. Sci., 30, pp. 1303-1326.

Madden, R. A. and E. J. Zipser, 1970: Multi-layered structure of the wind over the equatorial Pacific during the Line Island Experiment. J. Atmos. Sci., 27, pp. 336-342.

Phillips, N. A., 1966: The equation of motion for a shallow rotating Atmosphere and the "Tradidional Approximation". J. Atmos. Sci., 23, pp. 626-628.

Platt, C. M. R., 1973: Lidar and radiometric observations of cirrus clouds. J. Atmos. Sci., 30, pp. 1191-1204.

Reed, R. J. and E. E. Recker, 1971: Structure and properties of synoptic-scale wave disturbances in the equatorial Western Pacific. J. Atmos. Sci., 28, pp. 1117-1133.

Riehl, H., 1962: Radiation measurements over the Caribbean during the autumn of 1960. J. Geophys. Res., 67, pp. 3935-3942.

U. S. Committee on Extension to the Standard Atmosphere, 1966: U.S. Standard Atmosphere Supplements, 1966, U. S. Government Printing Office, Washington, D. C.

Wallace, J. M., 1970: Time-longitude sections of tropical cloudiness. ESSA Tech. Report NESC 56, Washington, D. C., July 1970, 37 pages.

Wallace, J. M., 1971: Spectral studies of tropospheric wave disturbances in the tropical Western Pacific. Rev. of Geophysics and Space Physics. 9, pp. 557-612.

Williams, K., 1970: A statistical analysis of satellite-observed trade wind cloud clusters in the western north Pacific. Dept. of Atmospheric Science Paper No. 161, Colorado State University.

Yamamoto, G., T. Masayuki, and S. Asano, 1970: Radiative transfer in water clouds in the infrared region. J. Atmos. Sci., 27, pp. 282-292.

REFERENCES - Continued

Yanai, M., S. Esbensen and J. Chu, 1973: Determination of bulk properties of tropical cloud clusters from large-scale heat and moisture budgets. J. Atmos. Sci., 30, pp. 611-627.

Zipser, E. and R. C. Taylow, 1968: A catalogue of meterological data obtained during the Line Island Experiment, February - April 1967. NCAR Technical Note TN-35, National Center for Atmospheric Research, Boulder, Colorado, 362 pages.

APPENDIX A: Derivation of Linearized Primitive Equations

The momentum equations in spherical coordinates (λ, ϕ, r) where r is the radius may be written as

$$\frac{du}{dt} = \left(2\Omega + \frac{u}{r \cos \phi}\right)(v \sin \phi - w \cos \phi) + F_\lambda, \tag{A.1}$$

$$\frac{dv}{dt} = -\left(2\Omega + \frac{u}{r \cos \phi}\right) u \sin \phi - \frac{wv}{r} + F_\phi, \tag{A.2}$$

and

$$\frac{dw}{dt} = \left(2\Omega + \frac{u}{r \cos \phi}\right) u \cos \phi - \frac{v^2}{r} + F_r - g. \tag{A.3}$$

F_λ, F_ϕ, and F_r represent the components of the pressure and frictional forces and g represents the gravitational acceleration and the centrifugal force due to the earth's angular velocity Ω. The velocities u, v and w are

$$\left.\begin{aligned} u &= h_\lambda \frac{d\lambda}{dt} \\ v &= h_\phi \frac{d\phi}{dt} \\ w &= h_r \frac{dr}{dt} \end{aligned}\right\}, \tag{A.4}$$

where the scale factors in (A.4) are

$$\left.\begin{aligned} h_\lambda &= r \cos \phi \\ h_\phi &= r \\ h_z &= 1 \end{aligned}\right\}. \tag{A.5}$$

The radius, r, may be represented as $r = a(1 + z/a)$ where z represents the vertical height above the sea level surface. Since the earth's atmosphere is relatively shallow compared to the radius of the earth, $z/a \ll 1$. Hence, to a first approximation, $r = a$ = constant and $dr = dz$.

Phillips (1966) has shown that if the approximation r = a is introduced into (A.5), and the resulting scale factors are used in the vector invariant form of the momentum equation

$$\frac{\partial \vec{V}}{\partial t} = \vec{F} + \vec{g} - \vec{\nabla}\left(\frac{1}{2}\vec{V}^2\right) + \vec{V}\times[\vec{\nabla}\times(\vec{V} + \vec{V}_e)]$$

where $$\vec{V}_e = \Omega h_\lambda \hat{i},$$

(A.1) to (A.3) may be written as

$$\frac{du}{dt} = \left(2\Omega + \frac{u}{a\cos\phi}\right) v \sin\phi + F_\lambda, \tag{A.6}$$

$$\frac{dv}{dt} = -\left(2\Omega + \frac{u}{a\cos\phi}\right) u \sin\phi + F_\phi, \tag{A.7}$$

$$\frac{dw}{dt} = F_z - g. \tag{A.8}$$

Although the terms $-\left(2\Omega + \frac{u}{a\cos\phi}\right) w\cos\phi$, $\frac{wv}{a}$, $2\Omega u\cos\phi$, and $\frac{u^2+v^2}{a}$ are missing in (A.6) to (A.8)[1], these equations satisfy the angular momentum principle

$$\frac{d}{dt}[a\cos\phi\,(u + \Omega a\cos\phi)] = a\cos\phi\, F_\lambda.$$

Equations (A.6) to (A.8), the continuity equation, and the first law of thermodynamics need to be expressed in terms of the pseudo-height coordinate system. Holton (1972) has discussed these transformations in detail.

In the pseudo-height coordinate system, the operator d/dt is defined as

$$\frac{d}{dt} = \frac{\partial}{\partial t} + \frac{u}{a\cos\phi}\frac{\partial}{\partial\lambda} + \frac{v}{a}\frac{\partial}{\partial\phi} + w\frac{\partial}{\partial z} \tag{A.9}$$

Using (A.9), (A.6) and (A.7) may be written as

---

[1] In hydrostatic problems, conservation of energy is enough to require that the w terms in (A.1) and (A.2) be dropped.

$$\frac{\partial u}{\partial t} + \frac{u}{a \cos \phi} \frac{\partial u}{\partial \lambda} + \frac{v}{a} \frac{\partial u}{\partial \phi} + w \frac{\partial u}{\partial \xi} =$$

$$\frac{uv}{a} \tan \phi - \frac{\partial \Phi}{a \cos \phi \, \partial \lambda} + 2\Omega \, v \sin \phi - \kappa u, \qquad (A.10)$$

$$\frac{\partial v}{\partial t} + \frac{u}{a \cos \phi} \frac{\partial v}{\partial \lambda} + \frac{v}{a} \frac{\partial v}{\partial \phi} + w \frac{\partial v}{\partial \xi} =$$

$$\frac{u^2 \phi}{a \tan \phi} - \frac{\partial \Phi}{a \, \partial \phi} - 2\Omega \, u \sin \phi - \kappa v, \qquad (A.11)$$

where the pressure and the frictional terms have replaced F_λ and F_ϕ.

If the motions are assumed to be hydrostatic, (A.8) in the pseudo-height system becomes

$$\frac{\partial \Phi}{\partial z} = \frac{RT}{H} \qquad (A.12)$$

where R is the gas constant for dry air. Similarly, the continuity equation and the first law of thermodynamics may be written as

$$\frac{1}{a \cos \phi} \frac{\partial u}{\partial \lambda} + \frac{1}{a} \frac{\partial v}{\partial \phi} - \frac{v}{a} \tan \phi + e^{\xi/H} \frac{\partial}{\partial \xi} (e^{-\xi/H} w) = 0 \qquad (A.13)$$

and

$$\frac{\partial T}{\partial t} + \frac{u}{a \cos \phi} \frac{\partial T}{\partial \lambda} + \frac{v}{a} \frac{\partial T}{\partial \phi} + w\left(\frac{R\overline{T}}{C_p H} + \frac{d\overline{T}}{d\xi}\right) = \frac{Q}{C_p} - \kappa T, \qquad (A.14)$$

where κT represents a Newtonian cooling factor and Q represents the remaining diabatic heating term.

The dependent variables in the equations described above may be expressed as follows:

$$\left.\begin{aligned}
u(\lambda, \phi, \xi, t) &= \overline{u}(\phi, \xi) + u'(\lambda, \phi, \xi, t) \\
v(\lambda, \phi, \xi, t) &= v'(\lambda, \phi, \xi, t) \\
w(\lambda, \phi, \xi, t) &= w'(\lambda, \phi, \xi, t) \\
\Phi(\lambda, \phi, \xi, t) &= \overline{\Phi}(\phi, \xi) + \Phi'(\lambda, \phi, \xi, t) \\
T(\lambda, \phi, \xi, t) &= \overline{T}(\phi, \xi) + T(\lambda, \phi, \xi, t) \\
Q(\lambda, \phi, \xi, t) &= \overline{Q}(\phi, \xi) + Q'(\lambda, \phi, \xi, t)
\end{aligned}\right\} \qquad (A.15)$$

where the barred quantities represent the time-zonally averaged basic state portion of the variables. The primed quantities in equation (A.15) represent the perturbation portion of the dependent variables. Substituting the variables defined in (A.15) into equations (A.10) to (A.14) and neglecting products of perturbation quantities, the resulting linearized equations may be written as

$$\frac{\partial u}{\partial t} + \frac{\bar{u}}{a \cos\phi}\frac{\partial u}{\partial \lambda} + w\frac{\partial \bar{u}}{\partial \xi} - \frac{v\bar{u}}{a}\tan\phi + \frac{v}{a}\frac{\partial \bar{u}}{\partial \phi} =$$

$$-\frac{\partial \Phi}{a \cos\phi \, \partial \lambda} + 2\Omega v \sin\phi - \kappa u \qquad \text{(A.16)}$$

$$\frac{\partial v}{\partial t} + \frac{\bar{u}}{a \cos\phi}\frac{\partial v}{\partial \lambda} + \frac{2u\bar{u}}{a}\tan\phi =$$

$$-\frac{\partial \Phi}{a \, \partial \phi} - 2\Omega u \sin\phi - \kappa v, \qquad \text{(A.17)}$$

$$\frac{\partial \Phi}{\partial \xi} = \frac{RT}{H}, \qquad \text{(A.18)}$$

$$\frac{1}{a \cos\phi}\frac{\partial u}{\partial \lambda} + \frac{1}{a}\frac{\partial v}{\partial \phi} - \frac{v}{a}\tan\phi + e^{\xi/H}\frac{\partial}{\partial \xi}\left(e^{-\xi/H}w\right) = 0 \qquad \text{(A.19)}$$

$$\frac{\partial T}{\partial t} + \frac{\bar{u}}{a \cos\phi}\frac{\partial T}{\partial \lambda} + \frac{v}{a}\frac{\partial \bar{T}}{\partial \phi} + w\left(\frac{R\bar{T}}{C_p H} + \frac{d\bar{T}}{d\xi}\right) = \frac{Q}{C_p} - \kappa T \qquad \text{(A.20)}$$

where the primes have been dropped on all primed quantities.

APPENDIX B

Numerical Solution of Second Order Partial Differential Equations

A method for solving a second order partial differential equation such as (2) is outlined by Lindzen and Kuo (1969).

The $y - \xi$ plane is discretized as shown in Figure B1. The unknown function $f(y, \xi)$ is defined at M x N points, making M x N unknowns. The original differential equation provides (M-2) x (N-2) equations. 2x(N-2) equations are provided by the boundary conditions at the y boundaries while 2M equations are provided by the boundary conditions at the ξ boundaries. Hence, to solve the equation, the M x N unknowns must be determined from the M x N equations described above.

The discrete form of the differential equation may be written as

$$\begin{aligned} &p(m, n)f(m, n-1) + q(m, n)f(m-1, n) \\ &+ r(m, n)f(m, n) + s(m, n)f(m+1, n) \\ &+ t(m, n)f(m, n+1) = u(m, n) \end{aligned} \qquad \text{(B.1)}$$

where

$m = 2, 3, \ldots M-1$

$n = 2, 3, \ldots N-1.$

The coefficients p, q, r, s, t, and the inhomogeneous term, u, are known from the original differential equation.

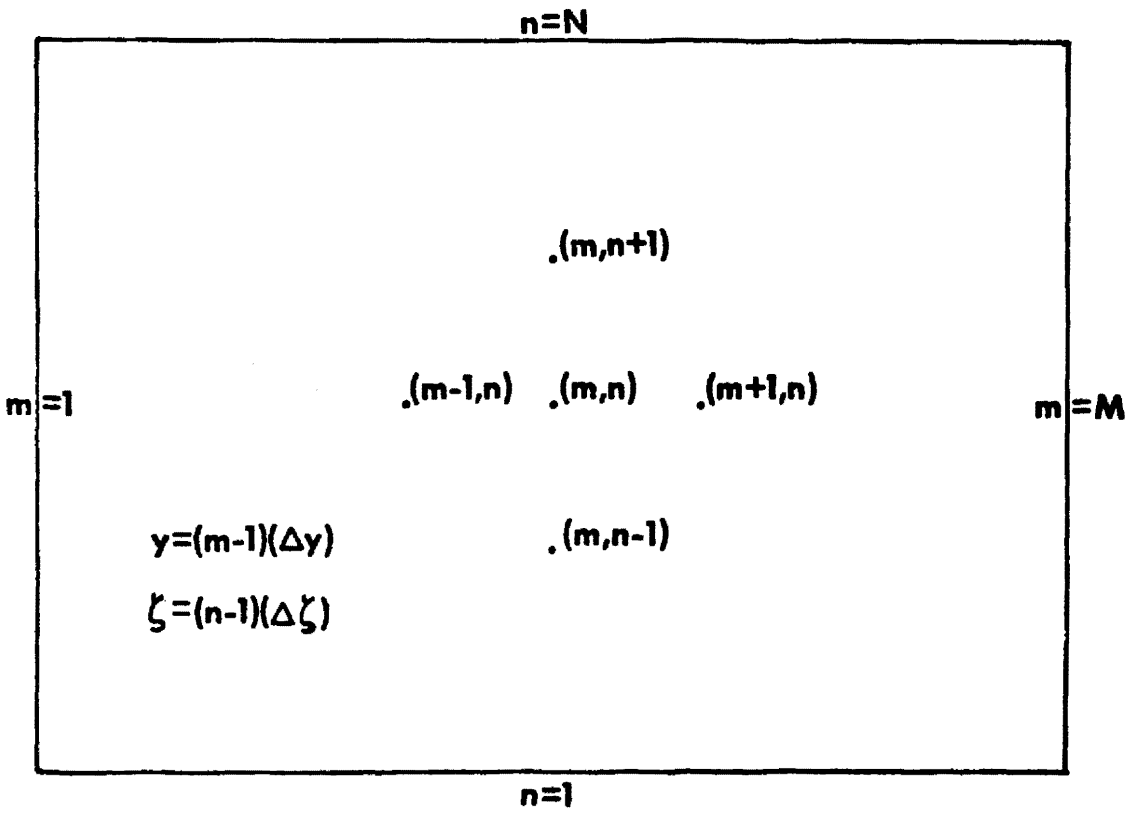

Figure B-1 - Sketch of discretized Y - ξ plane.

Equation B.1 may be written in vector form as

$$\begin{bmatrix} 0 & 0 & \cdots & 0 & 0 & 0 & \cdots & 0 & 0 \\ 0 & p(2,n) & \cdots & 0 & 0 & 0 & \cdots & 0 & 0 \\ \vdots & & \ddots & \vdots & \vdots & & & \vdots & \vdots \\ 0 & 0 & \cdots & p(m-1,n) & & & \cdots & 0 & 0 \\ 0 & 0 & \cdots & & p(m,n) & & \cdots & 0 & 0 \\ 0 & 0 & \cdots & & & p(m+1,n) & \cdots & 0 & 0 \\ \vdots & \vdots & & \vdots & \vdots & & \ddots & \vdots & \vdots \\ 0 & 0 & \cdots & 0 & 0 & 0 & \cdots & p(M,n) & 0 \\ 0 & 0 & \cdots & 0 & 0 & 0 & \cdots & 0 & 0 \end{bmatrix} \begin{bmatrix} f(1,n-1) \\ f(2,n-1) \\ \vdots \\ f(m-1,n-1) \\ f(m,n-1) \\ f(m+1,n-1) \\ \vdots \\ f(M-1,n-1) \\ f(M,n-1) \end{bmatrix} +$$

$$\begin{bmatrix} r(1,n)s(1,n) & \cdots & 0 & 0 & 0 & \cdots & 0 & 0 \\ q(2,n)r(2,n)s(2,n) & 0 & 0 & 0 & \cdots & 0 & 0 & \\ \vdots & \ddots & \vdots & \vdots & \vdots & & \vdots & \vdots \\ 0 & q(m-1,n)r(m-1,n)s(m-1,n) & & & \cdots & 0 & 0 & \\ 0 & 0 \cdots & q(m,n)r(m,n)s(m,n) & & \cdots & 0 & 0 & \\ 0 & 0 \cdots & & q(m+1,n)r(m+1,n)s(m+1,n) & & 0 & & \\ \vdots & \vdots & & \vdots & \ddots & \vdots & & \vdots \\ 0 & 0 \cdots & 0 & 0 & q(M-1,n)r(M-1,n)s(M-1,n) & & & \\ 0 & 0 \cdots & 0 & 0 & 0 \cdots & q(M,n)\,s(M,n) & & \end{bmatrix} \begin{bmatrix} f(1,n) \\ f(2,n) \\ \vdots \\ f(m-1,n) \\ f(m,n) \\ f(m+1,n) \\ \vdots \\ f(M-1,n) \\ f(M,n) \end{bmatrix} +$$

$$\begin{bmatrix} 0 & 0 & \cdots & 0 & 0 & 0 & \cdots & 0 & 0 \\ 0 & t(2,n) & \cdots & 0 & 0 & 0 & \cdots & 0 & 0 \\ \vdots & \vdots & \ddots & \vdots & \vdots & \vdots & & \vdots & \vdots \\ 0 & 0 & \cdots & t(m-1,n) & & & \cdots & 0 & 0 \\ 0 & 0 & \cdots & & t(m,n) & & \cdots & 0 & 0 \\ 0 & 0 & \cdots & & & t(m+1,n) & \cdots & 0 & 0 \\ \vdots & \vdots & & \vdots & \vdots & \vdots & \ddots & \vdots & \vdots \\ 0 & 0 & \cdots & 0 & 0 & 0 & \cdots & t(M-1,n) & 0 \\ 0 & 0 & \cdots & 0 & 0 & 0 & \cdots & 0 & 0 \end{bmatrix} \begin{bmatrix} f(1,n+1) \\ f(2,n+1) \\ \vdots \\ f(m-1,n+1) \\ f(m,n+1) \\ f(m+1,n+1) \\ \vdots \\ f(M-1,n+1) \\ f(M,n+1) \end{bmatrix} = \begin{bmatrix} u(1,n) \\ u(2,n) \\ \vdots \\ u(m-1,n) \\ u(m,n) \\ u(m+1,n) \\ \vdots \\ u(M-1,n) \\ u(M,n) \end{bmatrix}$$

where $n = 2, 3, \ldots N-1.$

Defining $\vec{f}_n \quad [f(1, n), f(2, n). \ . \ . \ . \ f(M, n)]$, (B.3)

and $\vec{D}_n \quad (u(1, n), u(2, n). \ . \ . \ . \ u(M, n)]$, (B.4)

B.2 may be written in the more compact form

$$A_n \vec{f}_{n-1} + B_n \vec{f}_n + C_n \vec{f}_{n+1} = \vec{D}_n \tag{B.5}$$

where A_n, B_n, and C_n are the appropriate matrices in (B.2).

The vector $\vec{f}_n$ may be expressed as

$$\vec{f}_n = \alpha_n \vec{f}_{n+1} + \vec{\beta}_n \tag{B.6}$$

where α_n is an unknown matrix and β_n is an unknown vector. Using (B.6) in (B.5), we obtain the relationships

$$(A_n \alpha_{n-1} + B_n) \alpha_n = - C_n \ , \tag{B.7}$$

and

$$(A_n \alpha_{n-1} + B_n) \vec{\beta}_n = \vec{D}_n - A_n \vec{\beta}_{n-1}. \tag{B.8}$$

If the boundary conditions at the lower and upper boundary may be written respectively as

$$\frac{\partial f}{\partial \xi} + a_b f = b_1 \ ,$$

and

$$\frac{\partial f}{\partial \xi} + a_t f = b_t \ ,$$

where a_b, b_b, a_t, b_t are constants, the boundary conditions in discrete vector form may be written as

$$A_b \vec{f}_1 + B_b \vec{f}_2 = \vec{D}_b \ , \tag{B.9}$$

and

$$A_t \vec{f}_{N-1} + B_t \vec{f}_N = \vec{D}_t. \tag{B.10}$$

The matrices A_b, B_b, A_t, B_t and the vectors $\vec{D}_b$ and $\vec{D}_t$ are known.

Comparing (B.9) with (B.6) we immediately obtain

$$A_b \alpha_1 = - B_b \tag{B.11}$$

and

$$A_b \vec{\beta}_1 = \vec{D}_b \ . \tag{B.12}$$

Hence, knowing α_1 and $\vec{\beta}_1$ from (B.11) and (B.12), (B.7) and (B.8) may be used to compute α_n and B_n for n = 2, . . . N-1.

Equations (B.8) and (B.6) may be used to derive the relationship

$$(B_t + A_t\alpha_{N-1})\,\vec{f}_N = D_t - A_t\,\vec{\beta}_{N-1}\,. \tag{B.13}$$

f_N is determined from this expression. Since α_n and β_n have been calculated, (B.6) may be used to calculate the remaining f_n.

To summarize the procedure, let us write (B.11), (B.12), (B.7), (B.8), (B.13) and (B.6) as

$$\alpha_1 = -A_b^{-1}B_b \tag{B.14}$$

$$\vec{\beta}_1 = A_b^{-1}\vec{D}_b \tag{B.15}$$

$$\alpha_n = -(A_n\,\alpha_{n-1} + B_n)^{-1}\,C_n \tag{B.16}$$

$$\vec{\beta}_n = (A_n\,\alpha_{n-1} + B_n)^{-1}\,(\vec{D}_n - A_n\vec{\beta}_{n-1}) \tag{B.17}$$

$$\vec{f}_N = (A_t\,\alpha_{N-1} + B_t)^{-1}\,(\vec{D}_t - A_t\vec{\beta}_{N-1}) \tag{B.18}$$

$$\vec{f}_n = \alpha_n\vec{f}_{n+1} + \vec{\beta}_n \tag{B.19}$$

Using (B.14) and (B.15) we determine α_1 and $\vec{\beta}_1$. Using (B.16) and (B.17) α_n and $\vec{\beta}_n$ are determined for n = 2, 3, . . . N-1. Using (B.18) we determine f_N, and using (B.19) we determine f_n for n = N-1, N-2, . . . 1. The solutions of linear algebraic systems (i.e. matrix inversions) were obtained by the procedures given in Forsythe and Moler (1967).

BIBLIOGRAPHIC DATA SHEET	1. Report No. CSU-ATSP-215	2.	3. Recipient's Accession No.

4. Title and Subtitle

The Large-Scale Response of the Tropical Atmosphere To Radiative Heating

5. Report Date: March 1974

6.

7. Author(s): Bruce A. Albrecht and Stephen K. Cox

8. Performing Organization Rept. No. CSU-ATSP-215

9. Performing Organization Name and Address

Department of Atmospheric Science
Colorado State University
Fort Collins, Colorado 80521

10. Project/Task/Work Unit No.

11. Contract/Grant No.

NSF GA-36302

12. Sponsoring Organization Name and Address

Atmospheric Science Section
National Science Foundation
Washington, D. C. 20550

13. Type of Report & Period Covered

M.S. Thesis

14.

15. Supplementary Notes

16. Abstracts

A large-scale diagnostic model is used to determine the effect of various diabatic forcing functions on tropospheric motions. Many of the features of the tropospheric equatorial waves are duplicated by using the observed difference in heating between the trough and the ridge of the waves in the model.

The structure of waves forced by the observed differences in radiative heating was determined. The atmospheric response was similar to the layered meridional wind structure observed during the Line Island Experiment. When the radiative heating was combined with convective heating, the vertical structure of the forced motions was found to be very sensitive to the phase difference between the convective and the radiative heating. The amplitude of the meridional wind perturbations at 200 mb varied from 1 m sec^{-1} for the case when radiatively active upper tropospheric clouds were centered over the convective heating to 5.5 m sec^{-1} when the cloud was centered a half of wavelength from the convective heating.

17. Key Words and Document Analysis. 17a. Descriptors

Tropical Waves

Easterly Waves

Atmospheric Radiation

Radiative Characteristics of Clouds

17b. Identifiers/Open-Ended Terms

17c. COSATI Field/Group

18. Availability Statement	19. Security Class (This Report) UNCLASSIFIED	21. No. of Pages
	20. Security Class (This Page UNCLASSIFIED	22. Price